Bone metastasis initiation is coupled with bone remodeling through osteogenic differentiation of NG2$^+$ cells

Weijie Zhang[1,2,3], Zhan Xu[1,2,3], Xiaoxin Hao[1,2,3], Tiancheng He[4], Jiasong Li[4], Yichao Shen[1,2,3], Kai Liu[4], Yang Gao[1,2,3], Jun Liu[1,2,3], David Edwards[1,2,3], Aaron M. Muscarella[1,2,3], Ling Wu[1,2,3], Liqun Yu[1,2,3], Longyong Xu[1,2,3], Xi Chen[1,2,3], Yi-Hsuan Wu[1,2,3], Igor L. Bado[1,2,3], Yunfeng Ding[1,2,3], Sergio Aguirre[1,2,3], Hai Wang[1,2,3], Zbigniew Gugala[5], Robert L Satcher[6], Stephen T. Wong[2,3,4], and Xiang H.-F. Zhang[1,2,3,7*].

[1]Lester and Sue Smith Breast Center, Baylor College of Medicine, Houston, TX 77030, USA
[2]Dan L. Duncan Cancer Center, Baylor College of Medicine, Houston, TX 77030, USA
[3]Department of Molecular and Cellular Biology, Baylor College of Medicine, Houston, TX 77030, USA
[4]Department of Systems Medicine and Bioengineering and Translational Biophotonics Laboratory, Houston Methodist Cancer Center, Houston, TX 77030, USA
[5]Department of Orthopedic Surgery & Rehabilitation, University of Texas Medical Branch, Galveston, TX 77555, USA
[6]Department of Orthopedic Oncology, University of Texas MD Anderson Cancer Center, Houston, TX 77030, USA.
[7]McNair Medical Institute, Baylor College of Medicine, Houston, TX 77030, USA
*Correspondence: Xiang H.-F. Zhang, mailing address: One Baylor Plaza, BCM 600, Houston, TX 77030; email: xiangz@bcm.edu; TEL: 713-798-6239.

RUNNING TITLE

NG2+ cells couple bone remodeling with metastasis initiation

KEYWORDS

Bone metastasis Initiation, Mesenchymal stromal/stem cells, Bone remodeling, NG2, N-cadherin

DECLARATION OF INTERESTS

The authors declare no potential conflicts of interest.

Downloaded from http://aacrjournals.org/cancerdiscovery/article-pdf/doi/10.1158/2159-8290.CD-22-0220/3217471/cd-22-0220.pdf by Washington University St Louis user on 10 November 2022

ABSTRACT

The bone microenvironment is dynamic and undergoes remodeling in normal and pathological conditions. Whether such remodeling impacts disseminated tumor cells and bone metastasis remains poorly understood. Here, we demonstrated that pathological fractures increase metastatic colonization around the injury. $NG2^+$ cells are a common participant of bone metastasis initiation and bone remodeling in both homeostatic and fractured conditions. $NG2^+$ bone mesenchymal stromal cells (BMSCs) often co-localize with DTCs in the perivascular niche. Both DTCs and $NG2^+$ BMSCs are recruited to remodeling sites. Ablation of $NG2^+$ lineage impaired bone remodeling and concurrently diminished metastatic colonization. In co-cultures, $NG2^+$ BMSCs, especially when undergoing osteo-differentiation, enhanced cancer cell proliferation and migration. Knockout of N-cadherin in $NG2^+$ cells abolished these effects *in vitro,* and phenocopied $NG2^+$ lineage depletion *in vivo*. These findings uncover dual roles of $NG2^+$ cells in metastasis and remodeling, and indicate that osteo-differentiation of BMSCs promotes metastasis initiation via N-cadherin-mediated cell-cell interaction.

SIGNIFICANCE

The bone colonization of cancer cells occurs in an environment that undergoes constant remodeling. Our study provides mechanistic insights into how bone homeostasis and pathological repair lead to outgrowth of disseminated cancer cells, thereby opening new directions for further etiological and epidemiological studies of tumor recurrences.

Downloaded from http://aacrjournals.org/cancerdiscovery/article-pdf/doi/10.1158/2159-8290.CD-22-0220/3217471/cd-22-0220.pdf by Washington University St Louis user on 10 November 2022

INTRODUCTION

Bone is frequently affected by metastasis of various cancer types (1–4), and bone metastases may further spread to multiple other organs (5). The diagnosis of bone metastasis is often relying on severe symptoms including pain and pathological fractures, which are driven by the vicious cycle between metastatic cells and bone-resorbing cells, osteoclasts (6–8). Specifically, cancer cells cooperate with osteoblasts to activate osteoclasts through multiple mechanisms (2,4,9). The bone resorption by osteoclasts releases a number of different grow factors from bone matrix, which in turn promote tumor growth and invasion. Based on this knowledge, current treatments target osteoclasts to slow down the vicious cycle and mitigate symptoms. However, further research is urgently needed to completely cure bone metastasis and prevent it from further disseminating to other organs.

Recent research has begun to unveil a prolonged period of asymptomatic phase. Before osteoclasts are recruited and activated, the perivascular and osteogenic niches may interact with metastatic seeds and regulate the dormancy and proliferation of DTCs, respectively (10–14). In particular, we have shown that the osteogenic cells and cancer cells can form heterotypic adherens junctions (hAJs) and gap junctions, which mediate the activation of mTOR signaling and calcium singling in cancer cells, respectively (11,12). Furthermore, the interaction with osteogenic cells also elicits global epigenomic reprogramming of cancer cells, leading to increase of phenotypic plasticity and empowering them for tertiary metastasis (5,15). However, the relationship between the perivascular niche and osteogenic niche remains elusive. One hypothesis is that they cooperate to initiate the progression from isolated DTCs to osteolytic metastases. Testing this hypothesis will shed light on etiology of metastatic recurrences, which often happen years to decades after removal of breast tumors

Bone is a highly dynamic organ even in adults (16). Under both homeostatic and pathological conditions, bone undergoes constant turnover (17). This process involves sequential migration, differentiation, proliferation, and cell-cell interactions of various cell types in the specialized bone remodeling compartments (BRCs), including mesenchymal stem cells (MSCs) and endothelial cells (18,19). Interestingly, there is a close interaction between endothelial cells and MSCs in the bone. Perivascular cells are considered as a major source of bone marrow MSCs (20), and endothelial cells appears to drive the differentiation of MSCs towards the osteoblastic lineages (21). After the initiation of bone remodeling, MSCs are recruited to BRCs via direct migration or circulation and coordinate both the resorption of old bone and formation of new bones through a precisely regulated differentiation process (18). Conceivably, those cellular activities lead to

Downloaded from http://aacrjournals.org/cancerdiscovery/article-pdf/doi/10.1158/2159-8290.CD-22-0220/3217471/cd-22-0220.pdf by Washington University St Louis user on 10 November 2022

disturbance in the bone microenvironment and might consequently alter DTC fate and kinetics of bone metastasis colonization. Herein, we tested this hypothesis by examining the connection between fracture-incurred bone remodeling and metastasis initiation.

RESULTS

To investigate the impact of bone remodeling on the progression of DTCs, we adopted a spontaneous metastasis model based on subcutaneous transplantation of Lewis Lung Carcinoma (LLC1) cells (22,23). The C57BL/6 background of this model enabled usage of several syngeneic mouse strains in which different subsets of bone cells can be genetically ablated or modified. 80% of tumor-bearing animals generated spontaneous bone metastases, which is substantially more frequent than other C57BL/6 cell line models we had examined (*i.e.*, <20% for TRAMP-C1, PYMT-E, PYMT-M and EO771 cells). Furthermore, expression of GFP and firefly luciferase in LLC1 cells did not result in immunogenic rejection of the cells or loss of these markers during tumor progression, which posed barriers in other models (24). Taken together, these advantages provided an unprecedented opportunity to examine how perturbation of specific BME components impacts microscopic metastases that spontaneously occur in immunocompetent hosts.

Fracture healing promotes spontaneous bone metastasis to the injured bone.

We used two approaches to introduce pathological bone fractures and stimulate consequent bone remodeling: drilling and bending, both of which have been used to study the wound-healing process of bone (25,26). Source tumors were implanted subcutaneously and reached 1 cm in diameter and approximately the same weight (Figure S1A, numeric values of all figures are provided in Supplementary Raw Data). Tumor resection and fracturing of right femur bones were then sequentially carried out on the same day (Figure 1A). Drilling and bending significantly increased metastasis frequency and tumor burden on the injured bone (Figure 1B-C), but not the contralateral unwounded bones (Figure 1C). The timing of bone injuries relative to resection of source tumors in these experiments indicated that the increased metastases were derived from DTCs already homing to bone.

Next, we examined the distribution of metastatic lesions along the femoral bone relative to the injury sites. Without pathological bone fractures, metastases predominantly localize to metaphyseal regions at the two ends of long bones. However, the bone fractures significantly skewed the distribution toward the injury sites (Figure 1B). Interestingly, although the less invasive drilling surgery only introduces an injury of 0.7 mm in diameter, the impact appeared to

Downloaded from http://aacrjournals.org/cancerdiscovery/article-pdf/doi/10.1158/2159-8290.CD-22-0220/3217471/cd-22-0220.pdf by Washington University St Louis user on 10 November 2022

spread to adjacent regions across the entire bone, similar to the pattern observed in invasive bending models (Figure 1D). This may be related to the fact that fractures often stimulate regional, rather than local, bone remodeling (27). Confocal microscopy and flow cytometry revealed an enrichment of GFP^+ cancer cells within the fractured area (Figure 1E-G and S1B). An increased proportion of cancer cells at the fracture site exhibited positive Ki67 staining while tumor cells in other parts of bone remained negative for Ki67 staining (Figure 1F). Indeed, Ki67+ cancer cells on average localized more closely to the fracture site (Figure S1C), and there is an inverse correlation between tumor burden and distance to the fracture site (Figure S1D), suggesting that fractures reprogram BME to promote proliferation of metastatic cells.

Bone fracture induces inflammation and bone repair. It was reported that inflammatory environment can promote outgrowth of cancer cells (28). To test this possibility, we performed immune cell profiling on drilled or bended areas of fractured bones 17 days after the procedure, but did not observe a significant change in the immune environment based on frequencies of major immune cell populations except the monocytes, B cells, and neutrophils in bending models (Figure 1H and S1E-F). In contrast, CD51+, PDGFRα+ and Sca-1+ cells with osteogenic potentials were enriched after fracturing (Figure 1I and S1G). While this data cannot rule out the effect of inflammation, we decided to first focus on cells of the osteogenic lineage. This decision was also based on our previous findings that the osteogenic niche plays critical roles in bone colonization under homeostatic conditions (11,12,15).

Depletion of $NG2^+$ cells impaired fracture-induced bone colonization.

In order to characterize the roles of various cells with osteogenic potentials in the BME, we crossed the ROSA26-LoxP-DTR (diphtheria toxin receptor) allele with Cre recombinase controlled by promoters of a number of widely studied markers of MSCs or skeletal stem cells (SSCs), including NG2, Nestin, and Leptin receptor (LepR). We also included Tie2-cre to examine potential roles of endothelial cells and the perivascular niche. Administration of DT (diphtheria toxin) reduced cells with expression of the respective Cre recombinase (Figure S2A-B).

Drilling was used to introduce focal fractures in femoral bones of animals of various strains. To more rapidly assess the ability of cancer cells to colonize the remodeling BME in multiple strains, we directly seeded cancer cells to the drilled sites and then monitored metastatic outgrowth by bioluminescence imaging (Figure 2A). Right after the seeding, we administered DT to ablate the corresponding cell populations. While reduction of $Nestin^+$ or $Tie2^+$ cells generated little effects on bone colonization at the wounded sites (Figure 2A), decrease of $NG2^+$ and $LepR^+$ cells

Downloaded from http://aacrjournals.org/cancerdiscovery/article-pdf/doi/10.1158/2159-8290.CD-22-0220/3217471/cd-22-0220.pdf by Washington University St Louis user on 10 November 2022

impeded bone colonization. LepR-cre is constitutively expressed during the development and its recombination activity labels both undifferentiated stem cells and differentiated lineages in adult animals, and depletion of LepR-cre$^+$ lineage by DT treatment leads to profound increase of adipocytes and osteoblasts (25), which makes LepR-cre not ideal for precise manipulation of bone marrow MSCs. On the other hand, NG2$^+$ perivascular cells are important stem/progenitor cells in the osteogenic lineage (29), and the NG2-cre strain used in this study is tamoxifen-inducible. Therefore, we decided to focus on NG2$^+$ cells in our subsequent investigations.

Using the mice with inducible NG2$^+$ lineage ablation as the hosts, we performed spontaneous metastasis assay. Specifically, source tumors were resected when reaching approximately the same weight (Figure S2C) and resection and bone-drilling were conducted on the same day (Figure 2B). Again, this setting allows us to focus on metastatic cells that already arrived at the time of fracture. The reduction of NG2-cre$^+$ cells significantly decreased spontaneous metastasis to the injured bone as shown by bioluminescence (Figure 2B and S2D) and flow cytometry of GFP$^+$ cancer cells (Figure S2E). Interestingly, metastasis to the contralateral un-injured bones was also decreased (Figure S2D), suggesting that NG2$^+$ cells may be important for metastasis under homeostatic conditions, which was tested in some later experiments. However, metastasis to lungs was not affected (Figure S2D), supporting the bone specificity of the role of NG2$^+$ cells.

We examined the spatial distribution of spontaneous metastatic lesions more closely. The enrichment of metastatic tumors surrounding the drilled site was clearly diminished by depletion of NG2$^+$ cells (Figure 2B-D). Importantly, NG2$^+$ depletion did not alter the immune cell profiles in the bone marrow (Figure S2F). Taken together, these data implicate NG2$^+$ MSCs as a major cell population driving bone colonization stimulated by remodeling.

Depletion of NG2$^+$ cells reduced bone colonization under homeostatic conditions.

Bone modeling is an ongoing process even under homeostatic conditions (17), albeit at a much lower rate compared to that during bone repair. We asked if NG2$^+$ cells also influence bone metastasis under homeostatic bone remodeling. We used the same spontaneous bone metastasis setting, i.e., DT treatment and source tumor resection were performed on the same day when implanted tumors reached a similar size (Figure 2E and S2G). Depletion of NG2$^+$ cells significantly hindered bone metastasis (Figure 2E-G) without affecting lung metastasis (Figure 2H). Under this homeostatic condition, depletion of Nestin$^+$ cells decreased the bone metastatic

Downloaded from http://aacrjournals.org/cancerdiscovery/article-pdf/doi/10.1158/2159-8290.CD-22-0220/3217471/cd-22-0220.pdf by Washington University St Louis user on 10 November 2022

burden but not the frequencies, while the reduction of spontaneous bone metastasis was not observed in other strains with depletion of LepR$^+$ and Tie2$^+$ cells (Figure S2H-P).

We next employed an experimental bone metastasis model based on intra-iliac artery (IIA) injection to directly deliver cancer cells to hind limb bones (30). This approach provides a definitive onset of bone colonization and is useful for characterizing the temporal course of this process (Figure 2I). NG2 depletion again exhibited significant decrease of metastatic burden in bone (Figure 2I). We noticed that the impact of NG2 depletion appeared from a very early stage of bone colonization (Figure 2I). To zoom into this phase, we carried out another experiment and administered DT prior to IIA implantation so that cancer cells immediately encountered a NG2-depleted BME upon arrival (Figure 2J). Depletion of NG2$^+$ cells showed no significant effects on the homing or survival of tumor cells to the bone, as determined by bioluminescence imaging and flow cytometry analysis of total, proliferative, or apoptotic tumor cells retrieved from bones 1 day after IIA injection (Figure S2Q-S). However, the lack of NG2$^+$ lineage significantly impaired the ability of DTCs, especially the Ki67+ fraction, to expand during the first six days of colonization (Figure 2J and S2T-V), confirming that the role of NG2$^+$ cells is more pronounced in bone metastasis initiation.

Taken together, the results so far indicate that the NG2$^+$ cells play the most consistent role in various metastasis assays and among all cell populations examined. Furthermore, this role appears to be important in both pathological and homeostatic conditions.

NG2$^+$ cells mediate osteogenesis and bone remodeling in homeostasis and fracture-healing conditions.

Given the roles of NG2$^+$ cells in bone remodeling-induced metastasis initiation, we wondered the normal functions of these cells in cancer-free bones. Although NG2-creER strain is often used to identify perivascular MSCs, there are other populations of MSCs that are characterized by other markers. Moreover, NG2 is also expressed to variable degrees by pericytes, chondrocytes, osteoblasts, osteocytes, Smooth muscle cells and peripheral nerve Schwann cells (20,25). Therefore, the precise cellular identity, spatial location and relative contribution of NG2-creER$^+$ cells to bone remodeling still need to be verified.

We first set out to analyze the differentiation potential of NG2-creER$^+$ cells. We employed NG2-creER;ROSA26-LoxP-TdTomato mice, in which cells expressing NG2-creER and their decedent cells will express TdTomato permanently (designed as NG2-tdRED$^+$ hereafter for brevity) and can be then purified from these mice for *in vitro* characterization (Figure 3A). NG2-tdRED$^+$ cells

Downloaded from http://aacrjournals.org/cancerdiscovery/article-pdf/doi/10.1158/2159-8290.CD-22-0220/3217471/cd-22-0220.pdf by Washington University St Louis user on 10 November 2022

are more frequent in the endosteal bones and needs to be extracted by enzymatic digestion (Figure S3A). In culture conditions favoring differentiation toward different lineages, NG2-tdRED$^+$ cells became osteoblasts, adipocytes and chondrocytes and therefore met the *in vitro* criteria of MSCs. However, compared to the NG2-tdRED$^-$ counterparts, NG2-tdRED$^+$ cells clearly exhibited a strong commitment toward osteolineage and a slightly increased adipogenic differentiation capacity (Figure 3B and S3B). PDGFRα$^+$CD51$^+$ stromal cells have been demonstrated to contribute to the majority of fibroblastic colony formation units (CFU) in bone marrow cells and represent a subset with greater self-renew capacity *in vivo* (31). Nestin-GFP$^+$ MSCs largely overlap with PDGFRα$^+$CD51$^+$ subset and NG2 protein markers its perivascular subpopulation, which also contains most CFU-F of bone marrow stromal cells in mice (32). NG2-tdRED$^+$ cells enriched PDGFRα$^+$CD51$^+$ fraction, possessed higher expression levels of self-renewal genes *Pou5f1* and *Sox2*, and showed the enhanced CFU-F activities compared to the NG2-tdRED$^-$ population (Figure S3C-F).

We next performed a lineage-tracing experiment by combining the osteocalcin-GFP (OCN-GFP) allele with NG2-creER;ROSA26-LoxP-TdTomato strain. Theoretically, a short period of tamoxifen treatment could induce the recombinase activity mainly in the NG2$^+$ progenitor cells and their progeny cells would inherit the expression of tdRED reporter. Osteocalcin is specifically expressed by mature osteoblasts, and therefore this lineage tracing model allows the identification of NG2-creER derived osteoblasts (tdRED$^+$GFP$^+$) and other non-NG2-creER derived osteoblasts (tdRED$^-$GFP$^+$) (33). We examined cells double positive for OCN-GFP and NG2-tdRED at different time points after a brief 5-day tamoxifen induction of NG2-creER activity by either immunofluorescent staining or flow cytometry. Under the homeostatic condition, double positive cells were rare 2 days after the tamoxifen induction (Figure 3C-D and S3G-H), suggesting minimal leakage of cre activity in existing osteoblasts post induction. This population became apparent later and remained at a relatively constant level for more than four months (Figure 3C-D and S3G-H). The majority of NG2-tdRED$^+$ cells remain negative for OCN-GFP, suggesting a potentially strong self-renewal capacity of NG2$^+$ stromal cells (Figure S3G). Importantly, over 20-50% of all the OCN-GFP$^+$ osteoblasts were also positive for NG2-tdRED 4 weeks after induction (Figure 3D and S3I), indicating a substantial proportion of new osteoblasts are decedents of NG2$^+$ MSCs. Furthermore, there was a high concordance between non-differentiated NG2-tdRED$^+$ cells and NG2 protein expression (Figure S3J), as well as another MSC marker LepR (25) and pericyte marker PDGFRβ (34) (Figure S3K-L). Interestingly, there was minimal overlap between NG2-tdRED and chondrocyte or adipocyte marker (Aggrecan or Perilipin, respectively) (25) (Figure S3M). In addition, about 30% of LepR-tdRED$^+$ cells were

Downloaded from http://aacrjournals.org/cancerdiscovery/article-pdf/doi/10.1158/2159-8290.CD-22-0220/3217471/cd-22-0220.pdf by Washington University St Louis user on 10 November 2022

also stained positively with NG2 antibody by flow cytometry (Figure S3N). Immunofluorescent staining showed that perivascular LepR-tdRED$^+$ cells also express NG2 protein in endosteal and fracture regions but not bone marrow cavity (Figure S3O). Taken together, the lineage-tracing results strongly support that NG2-tdRED$^+$ cells are MSC-like cells committed for osteogenic differentiation and represent a major contributor to bone remodeling.

We then examined the impact of NG2$^+$ cell depletion on bone remodeling. Using NG2-creER; ROSA26-LoxP-DTR mice, administration of DT reduced the osteogenic lineages marked by either CD51$^+$, PDGFRα$^+$, or Sca-1$^+$ cells (Figure S3P), suggesting a shrinkage of cell reservoir with osteogenic potentials. The ablation of NG2$^+$ cells also led to decrease of both osteoblast and osteoclast activities (Figure 3E-H), and reduced rate of new bone formation (Figure 3I-J). Thus, NG2$^+$ MSCs play a critical role in bone remodeling under normal conditions.

Finally, we used the same lineage tracing and depletion systems to study the roles of NG2$^+$ cells in repair of pathological fractures. Indeed, it is evident that NG2-tdRED$^+$ cells were recruited to callus and participated in the generation of new bones (Figure 3K). It has been reported that *in vivo* transplanted MSCs can engraft the bone and modulate bone-related pathogenesis and regeneration (35–37). To test whether NG2$^+$ cells exert similar functions, we sorted out and injected NG2-tdRED$^+$ bone stromal cells into the femoral cavity of wild-type mice, which procedure also created a defect extending from the articular cartilage to the femoral medullary cavity. 10 days post-surgery, the bones received transplantation of NG2-tdRED$^+$ cells exhibited a slight increase of new bone volume and a significant increase of new bone surface at the injured metaphyseal region (Figure S3Q-S), in comparison to the sham control femurs which were injected with saline. In line with previous reports (38,39), NG2-tdRED$^+$ cells were observed at the injured and other bone regions, and part of them also differentiated into mature osteoblasts (stained positively with osteocalcin) (Figure S3T). Moreover, loss of NG2$^+$ cells by DT treatment resulted in significantly delayed bone repair in drilling models (Figure 3L-M). Therefore, NG2$^+$ MSCs also appear to mediate bone remodeling during repair of pathological fractures.

Spatial distribution of DTCs and NG2$^+$ cells in early-stage bone metastasis.

We asked if the early impact of NG2$^+$ cells on bone metastasis is reflected by their spatial distributions relative to DTCs using NG2-creER;ROSA26-LoxP-TdTomato mice. By adopting a tissue clarity approach (Figure 4A), we were able to perform confocal microscopy and reconstruct 3D images of entire femur bones, and detect single DTCs and microscopic metastases that occur spontaneously (Figure 4B) or experimentally introduced by IIA (Figure

Downloaded from http://aacrjournals.org/cancerdiscovery/article-pdf/doi/10.1158/2159-8290.CD-22-0220/3217471/cd-22-0220.pdf by Washington University St Louis user on 10 November 2022

4C). In both cases, cancer cells were found more frequently in endosteal region compared to central bone marrow, and very often co-localized with NG2-tdRED$^+$ cells (Figure 4B-C). At a single-cell resolution, many cancer cells appeared to reside in the perivascular niche with or without direct contact with NG2-tdRED$^+$ perivascular cells (Figure S4A). Some cancer cells even develop prolonged protrusions that connect NG2-tdRED$^+$ cells (Figure S4A), resembling a unique cell-cell interaction we previously observed *in vitro* (40). We also employed a computational approach to quantitate distribution of DTCs and NG2-tdRED$^+$ cells relative to each other in early stage of synchronized bone colonization introduced by IIA. Compared to random simulated locations, the distance between the two cell populations was significantly shorter (Figure 4D and S4B). When the same analysis was applied to endothelial cells, we did not observe similar results (Figure S4C-D). As DTCs progress into microscopic metastases, there appeared to be an inverse correlation between the size of metastasis and distance to NG2-tdRED$^+$ cells (Figure S4E). DTCs in NG2$^+$ lineage depleted animals were rare and mostly single cells (Figure S4F), but about 70% of them remained close to endothelial cells as compared to NG2-tdRED$^+$ cells (Figure S4G-I), suggesting depletion of NG2$^+$ cells does not alter the perivascular location of tumor cells. Finally, pathological fractures by drilling or bending led to enrichment of both cancer cells and NG2-tdRED$^+$ cells, as well as extensive direct cell-cell interactions between the two cell populations (Figure 4E).

Taken together, our data reveal a spatial correlation between DTCs and NG2$^+$ cells, and uncover frequent and direct contact between these cell types during bone metastasis progression.

NG2$^+$ BMSCs promote cancer cell proliferation and migration in a cell-cell contact-dependent manner.

The frequent and direct contact between DTCs and NG2$^+$ cells during bone colonization prompted us to inspect their interactions in a simplified system and for a broader scope of cancer models. We selected nine murine cancer cell lines including LLC1 used in previous experiments. These lines represent five different cancer types and two genetic backgrounds. We admixed these lines with primary NG2-tdRED$^+$ BMSCs freshly purified from syngeneic NG2-creER;ROSA26-LoxP-TdTomato mice after tamoxifen induction. BMSCs that do not express NG2-tdRED from same mice were also prepared for comparison. In 3D suspension cultures, the vast majority of cancer models formed heterotypic organoids with NG2-tdRED$^+$ cells (Figure 5A). Some are very similar to what we observed before using human cancer cells and MSCs (12), including 4T1.2, CMT93, EMT6, LLC1 and PYMT-E cells. Most models benefited from

Downloaded from http://aacrjournals.org/cancerdiscovery/article-pdf/doi/10.1158/2159-8290.CD-22-0220/3217471/cd-22-0220.pdf by Washington University St Louis user on 10 November 2022

interaction with both NG2-tdRED$^+$ and NG2-tdRED$^-$ BMSCs except EO771 cells (Figure 5B). In four models (CMT93, EMT6, LLC1 and PYMT-E), NG2-tdRED$^+$ cells conferred a significantly stronger advantage compared to the NG2-tdRED$^-$ counterparts (Figure 5B). This difference appeared to be dependent on cell-cell contact, as separation of BMSCs and cancer cells by Boyden Chambers largely diminished the extra cancer-promoting effects by NG2-tdRED$^+$ cells (Figure S5A). The interaction with NG2-tdRED$^+$ BMSCs promoted cancer cell proliferation as indicated by increased percentage of Ki67$^+$ proliferating tumor cells in organoids formed by LLC1 tumor cells and BMSCs (Figure 5C-D). Real-time imaging in 2D co-cultures also revealed that cancer cells rapidly established cell-cell contact with NG2-tdRED$^+$ BMSCs and developed colonies surrounding these cells (Supplementary Video 1), and the size of colonies was significantly larger compared to co-cultures with NG2-tdRED$^-$ BMSCs and monocultures (Figure 5E-F, and Supplementary Video 2, 3). In fact, LLC1 cells could not grow without BMSCs in serum-free condition. Furthermore, within the same co-culture, colonies maintaining direct contact with NG2-tdRED$^+$ BMSCs were significantly larger than those losing direct contact (Figure S5B-C), albeit the numbers of colonies did not differ between these two situations (Figure S5D).

The direct contact with NG2-tdRED$^+$ BMSCs not only promotes proliferation of cancer cells, but also enhances their movement as shown in a trans-well migration assay. Specifically, GFP$^+$ cancer cells were admixed with BMSCs in the upper level of the Boyden Chamber. The trans-well migration of cancer cells appeared to be greatly enhanced by the presence of NG2-tdRED$^+$ BMSCs as compared to NG2-tdRED$^-$ BMSCs (Figure 5G-H).

Finally, the tumor-promoting effects of NG2-tdRED$^+$ BMSCs were even stronger when BMSCs were pretreated with medium favoring osteo-differentiation except for B16F10 cells (Figure 5I and S5E-F). This extra effect was not observed for most tumor cells when co-culturing with NG2-tdRED$^-$ BMSCs (Figure 5I), and was critically dependent on cell-cell contact (Figure S5G).

Taken together, the *in vitro* co-culture experiments uncover a superior ability of NG2$^+$ cells in promoting tumor progression compared to other BMSCs. Importantly, this effect appears to be relying on direct cell-cell contact, and becomes further strengthened upon osteo-differentiation.

N-cadherin expressed on NG2+ cells mediates both bone remodeling and fracture-induced metastatic colonization

Our previous studies demonstrated that cancer cells form heterotypic adherens junctions (hAJs) with the osteogenic niche cells in early-stage bone colonization. E-cadherin from cancer cells

Downloaded from http://aacrjournals.org/cancerdiscovery/article-pdf/doi/10.1158/2159-8290.CD-22-0220/3217471/cd-22-0220.pdf by Washington University St Louis user on 10 November 2022

and N-cadherin from the osteogenic cells constitute hAJs (11,12), which can also be observed in heterotypic organoids formed by E-cadherin$^+$ mouse tumor cells (4T1.2, CMT93, EMT6, LLC1 and PYMT-E) and NG2-tdRED$^+$ BMSCs (Figure S5H). Consistently, four (CMT93, EMT6, LLC1 and PYMT-E) of these tumor cells, which gained additional growth benefit, showed elevated level of phosphorylated S6 kinase upon co-culture with NG2$^+$ BMSCs, indicating activation of mTOR signaling in these cells when interacting with NG2$^+$ BMSCs (Figure S5I-J). Knockdown of E-cadherin on tumor cells by siRNAs significantly diminished the growth promotion effect of both NG2$^-$ and NG2$^+$ BMSCs in these cells, under either normal medium or osteo-differentiation medium (Figure S6A). In this study, direct cell-cell contact again appeared to be critical in determining the roles of NG2$^+$ cells, which enriches stem cells committed for osteogenesis. In support of this notion, transient knockdown of N-cadherin by siRNAs on both NG2$^-$ and NG2$^+$ BMSCs also blocked their growth promotion effects to E-cadherin$^+$ tumor cells (Figure S6B). We found that N-cadherin was expressed at a higher level in NG2-tdRED$^+$ cells compared to NG2-tdRED$^-$ BMSCs (Figure S3D), and its expression was further increased during *in vitro* osteogenic differentiation in NG2$^+$ cells (Figure S5F), both of which support an important role of N-cadherin in osteoblast differentiation and osteogenesis (41–43). Interestingly, a recent report suggested that N-cadherin$^+$ stromal cells share similar transcriptomic profile with NG2$^+$ cells and are the main source of bone and marrow stromal progenitor cells (44), so we reasoned that knockout of N-cadherin expression in these cells may disrupt the interaction between NG2$^+$ cells and cancer cells, thereby abolishing the effects of bone remodeling on metastasis initiation. To test this hypothesis, we bred NG2-creER;LoxP-CDH2 mice to delete N-cadherin selectively in NG2-cre$^+$ cells in an inducible fashion (designed NG2-Ncad$^{KO/KO}$ hereafter) (Figure S6C). Indeed, N-cadherin was significantly reduced in NG2-tdRED$^+$ cells from NG2-Ncad$^{KO/KO}$ mice (Figure S6D-E).

We first asked if depletion of N-cadherin also influences the normal function of NG2$^+$ cells. *In vitro* differentiation assays revealed notable decrease of osteo-differentiation as well as adipo-differentiation upon N-cadherin knockout (Figure S6F, compared to Figure 3B and S3B). Loss of N-cadherin in NG2$^+$ cells also decreased bone mineralization rate (Figure 6A-B) and slowed down repair of bone fracture (Figure 6C-D). These data together demonstrate the pivotal role of N-cadherin in homeostatic and pathological bone remodeling.

We next examined whether loss of N-cadherin affects the cancer-promoting effects in NG2$^+$ cells in co-cultures. NG2-tdRED$^+$ cells were also extracted NG2-Ncad$^{KO/KO}$ mice (referred as KO BMSCs hereafter), and were admixed with a variety of cancer models in parallel with the

Downloaded from http://aacrjournals.org/cancerdiscovery/article-pdf/doi/10.1158/2159-8290.CD-22-0220/3217471/cd-22-0220.pdf by Washington University St Louis user on 10 November 2022

previously isolated wildtype NG2-tdRED^{+} cells (hereafter referred as WT BMSCs for simplicity) in above-mentioned *in vitro* co-culture experiments. Only the seven C57BL/6 cancer cells were tested because NG2-Ncad$^{KO/KO}$ is only available in this genetic background. In five of the tested models, a significant reduction of tumor-promoting effect was observed (Figure 6E). In addition, the levels of phosphorylated S6K were also reduced in PYMT-E, CMT93, LLC1 tumor cells co-cultured with KO cells (Figure S5J). Further experiments uncovered a decrease of Ki67^{+} cells in the 3D heterotypic organoids (Figure 6F-G) and an overall decrease of colony size in 2D co-cultures using LLC1 cells co-cultured with KO cells (Figure 6H-I and Supplementary Video 4). When the analysis was restricted to the cancer cells maintained the direct contact with NG2-tdRED^{+} cells, knockout of N-cadherin clearly diminished colony size (Figure S6G). However, this difference was not found for colonies that were not in firmly contact with WT or KO NG2-tdRED^{+} cells (Figure S6H). Loss of N-cadherin also impaired the migration of both cancer cells (Figure 6J-K) and NG2-tdRED^{+} cells (Figure S6I). In addition, the excessive cancer-promoting effect stimulated by osteo-differentiation was also abolished by N-cadherin knockout especially in the 3D co-cultures (Figure 6L and S6J). Thus, N-cadherin in NG2^{+} cells is responsible for the superior ability of these cells in promoting cancer proliferation and migration *in vitro*.

We set out to determine the impact of NG2-specific knockout of N-cadherin on bone metastasis. Two different experiments were performed toward this end. In the first experiment, cancer cells were directly inoculated into drilled bones in either Ncad$^{WT/WT}$ or NG2-Ncad$^{KO/KO}$ mice. The cancer cell growth was significantly impaired in NG2-Ncad$^{KO/KO}$ animals (Figure 6M). In addition to bioluminescence quantitation, we also enumerated GFP^{+} cancer cells on the drilled site by flow cytometry and confirmed the difference in tumor progression between Ncad$^{WT/WT}$ and NG2-Ncad$^{KO/KO}$ animals (Figure S6K). Thus, N-cadherin in NG2^{+} cells is critical for the outgrowth of already seeded cancer cells. The second experiment is a spontaneous bone metastasis assay. We carried out bone-drilling on the same day of source tumor resection, and monitored development of spontaneous bone metastasis (Figure 6N). We did not observe difference in primary tumor growth (Figure S6L). However, N-cadherin knockout in NG2^{+} cells significantly decreased metastasis surrounding the drilled site (Figure 6N-P). In contrast, there were no significant differences in metastasis to contralateral, non-injured bones or to lung (Figure S6M). Taken together, these data strongly support a critical role of N-cadherin in NG2^{+} cells during bone remodeling-stimulated metastasis.

Finally, we examined if knockout of N-cadherin in NG2^{+} cells may affect drilling-associated inflammation. A flow cytometry-based characterization of immune cell profile did not detect any

Downloaded from http://aacrjournals.org/cancerdiscovery/article-pdf/doi/10.1158/2159-8290.CD-22-0220/3217471/cd-22-0220.pdf by Washington University St Louis user on 10 November 2022

significant alterations to the major populations (Figure S6N). Thus, although our data cannot directly rule out the influence from inflammation, the observed roles of $NG2^+$ cells and N-cadherin in $NG2^+$ cells do not seem to be mediated by alteration of immune cells.

Correlative analyses human metastases support the connection between osteogenic differentiation and bone colonization.

We examined the *in situ* protein expression of NG2 and N-cadherin in a small number of human bone metastases from various types of cancer including breast, prostate, colon and lung cancers, and confirmed that NG2 and N-cadherin were both expressed by cells surrounding metastatic cells (Figure 7A). To gain deeper insight into the functional relevance of $NG2^+$ cells in human bone metastasis, we compared NG2 expression (encoded by gene CSPG4) in solid bone tumor tissues (Tumor) versus matched liquid bone marrow involved in the metastases (Involved) or in a different bone (Distal), as well as bone marrow samples from tumor-free patients (Benign) from a single cell RNA-seq (scRNA-seq) dataset of prostate bone metastases (45). A significantly higher level of NG2 expression was observed in tumor tissues (Figure 7B). To determine whether the NG2 expression is specific to perivascular mesenchymal cells, we examined the co-expression of NG2 and other cell type-characteristic genes. Indeed, $NG2^+$ cells also express RGS5, ACTA2 and PGF, the well-established pericyte markers (46), but not with cancer cell-specific genes such as AR and KLK3 (Figure 7C). Further analyses revealed that the frequency of $NG2^+$ perivascular cells correlated with tumor-proliferation index (47) (Figure 7D) and N-cadherin-related osteoblast differentiation signature (48) (Figure 7E), supporting our hypothesis that $NG2^+$ cells drive both osteogenesis and tumor progression.

Since NG2 expression in bone metastasis is mainly contributed by perivascular mesenchymal cells, we set out to analyze a larger number of bone metastases in more cancer types using bulk RNA-seq data. In two datasets comprising metastases at different sites, we observed that NG2 expression is significantly higher in bone metastases of both breast and prostate cancers (Figure S7A). Moreover, among bone metastases, NG2 expression exhibits significant correlations with N-cadherin expression and a gene expression signature indicative of osteoblast differentiation (Figure S7B-C). Interestingly, such correlation was not observed in other metastases or primary tumors (Figure S7D). In breast cancer bone metastases, NG2 is also associated with increase of EZH2, increase of an embryonic stem cell signature overexpressed in aggressive tumors, and decrease of ESR1 expression and related gene expression signatures (Figure 7F). This is consistent with our previous finding that direct interaction with osteogenic cells promotes the phenotypic plasticity of cancer cells in the bone

Downloaded from http://aacrjournals.org/cancerdiscovery/article-pdf/doi/10.1158/2159-8290.CD-22-0220/3217471/cd-22-0220.pdf by Washington University St Louis user on 10 November 2022

microenvironment (5,15). In prostate cancer bone metastases, non-AR-driven tumors exhibited a remarkably higher expression of NG2 (Figure 7G), suggesting that crosstalk with osteogenic cells may activate alternative pathways to drive tumor progression. Taken together, our data support an important role of NG2+ perivascular cells in bone metastasis progression.

DISCUSSION

The BME comprises of many different cell types that are intricately organized (1). Even cells of seemingly the same type may be functionally and molecularly distinct depending on their geographic locations, cell-of-origins, and interacting cells. For example, Lin *et al.* has shown the critical role of endothelial cells-converted osteoblasts in the formation of osteoblastic metastases of prostate cancer (49). Mesenchymal stem cells represent another great example of this kind. The exact identity and functions of MSCs have been intensively studied (20). Different subpopulations of MSCs may vary in their roles in homeostatic vs. pathological conditions, their differentiation capacity to different lineages *in vitro* and *in vivo*, and their location relative to vasculature and endosteum (50,51). In this study, we identified a unique role of NG2-creER$^+$ cells, which are presumably a subset of MSCs. Previous studies have elucidated that NG2$^+$ cells predominantly localize at the metaphysis and H-type vasculature in the bone, where osteogenesis and angiogenesis are coupled (29). On the other hand, most DTCs were found in the same area. Indeed, we and others both discovered co-localization between NG2$^+$ cells and DTCs in the perivascular niche (13,14). Moreover, a recent work by Yip et al. found that disseminated breast cancer cells preferentially co-localize with H-type vessels in bone and tumor-derived G-CSF remodels the bone marrow vasculatures to resemble H-type vessels and therefore supports the metastatic growth in bone (52). Interestingly, NG2$^+$ BMSCs appear to express a higher level of N-cadherin, a component of heterotypic adherens junction with cancer cells (11,12). Thus, both geographic location and cancer-interacting molecule may distinguish NG2$^+$ MSCs from the other MSCs.

Our work highlights the dynamic nature of BME. Various microenvironment niches have been implicated in metastasis, including the perivascular niche and the osteogenic niche. However, the potential connection between these niches remains elusive. NG2$^+$ MSCs localize in perivascular niche in the resting stage, but can become mobilized and participate in osteogenesis during bone remodeling (19). Thus, it is conceivable that these cells may connect different niches. Our recent work suggested that cancer cells can migrate by tethering MSCs with a unique cellular protrusion (40). In this study, we also found that direct interaction with NG2$^+$ cells stimulate cancer cell migration toward osteogenic signals. These data postulate an

Downloaded from http://aacrjournals.org/cancerdiscovery/article-pdf/doi/10.1158/2159-8290.CD-22-0220/3217471/cd-22-0220.pdf by Washington University St Louis user on 10 November 2022

interesting hypothesis that cancer cells in the perivascular niche may "ride" $NG2^+$ MSCs and be co-recruited to sites of remodeling, thereby leaving one niche for another. This hypothesis will need to be tested *in vivo* ideally by real-time microscopy in future studies.

The dynamics of BME and $NG2^+$ cells may also reconcile the seemingly contradictory results between this and a previous study. Nobre *et al.* showed that bone marrow $NG2^+Nestin^+$ perivascular MSCs enforce dormancy of EO771 cells through secretion of TGFβ2 (53). The biological contexts examined in the two studies are different. Whereas Nobre *et al.* focused on the role of resting $NG2^+Nestin^+$ cells in the perivascular niche, our study predominantly examined remodeling-activated $NG2^+$ cells that couple bone metastasis progression with development of the osteogenic niche. In addition, the discrepancy may also partly result from intrinsic differences among cancer models. The EO771 cells do not express E-cadherin, and therefore did not form heterotypic adhesion junctions with N-cadherin$^+$ BMSCs and subsequently could not gain proliferative advantage in co-cultures with $NG2^+$ cells in our experiments, which is in contrast to LLC1 and a few other models, suggesting different cell-cell interaction mechanisms.

The connection between bone turnover and bone metastasis can explain some circumstantial epidemiological observations. For instance, Obi *et al.* observed an increased risk of bone metastasis related to fracture events in a large cohort of breast cancer survivors (54). There are also cases that breast or lung cancer spreads to the rare sites, such as the oral cavity and the jaws, in patients receiving dental implants (55–58), further indicating the potential connection between bone remodeling and the emergence of metastatic disease. Therefore, our discovery provides one potential mechanistic explanation for these clinical observations: bone remodeling stimulates osteodifferentiation, and DTCs may take advantage of this process and become invigorated through direct interaction with $NG2^+$ MSCs. Further epidemiology studies will be needed for more in-depth investigation on links between bone metastasis and other life events that alter bone turnover rate.

Downloaded from http://aacrjournals.org/cancerdiscovery/article-pdf/doi/10.1158/2159-8290.CD-22-0220/3217471/cd-22-0220.pdf by Washington University St Louis user on 10 November 2022

MATERIALS AND METHODS

Cell Lines and Cell Culture

Mouse melanoma cells B16-F10 (C57BL, Cat# CRL-6475, RRID: CVCL_0159), rectal carcinoma cells CMT-93 (C57BL, Cat# CCL-223, RRID: CVCL_1986), breast cancer cells EMT6 (BALB/c, Cat# CRL-2755, RRID: CVCL_1923), EO771 (C57BL, Cat# CRL-3461, RRID: CVCL_GR23), Lewis lung carcinoma cells LLC1 (C57BL, Cat# CRL-1642, RRID: CVCL_4358), prostate cancer cells TRAMP-C1 (C57BL, Cat# CRL-2730, RRID: CVCL_3614) were obtained directly from ATCC. 4T1.2 (BALB/c, RRID: CVCL_GR32) and AT-3 (C57BL, RRID:CVCL_VR89) cells were kindly provided by Dr. Robin Anderson (ONJCRI) and Dr. Ekrem Emrah Er (UIC), respectively. PyMT-E (C57BL, RRID: N/A) is a subline generated from MMTV-PyMT tumors in our lab as previously described (59). B16-F10, CMT-93, 4T1.2, LLC1, AT-3, PyMT-E cells were maintained in DMEM high glucose media (HyClone) supplemented with 10% FBS (Gibco); EMT6 cells were maintained in Waymouth's MB medium (Gibco) with 15% FBS; EO771 cells were cultured in RPMI-1640 medium (HyClone) supplemented with 10mM HEPES (Gibco) and 10% FBS; TRAMP-C1 cells were cultured in DMEM high glucose media supplemented with 5mg/L bovine insulin (Sigma), 10nM dehydroisoandrosterone (ACROS Organics) and 10% FBS. All the media were supplemented with 1% penicillin-streptomycin (Lonza) and cells were cultured in 5% CO2 incubator. EO771, LLC1, AT-3 cells were authenticated by STR profiling provided by ATCC. Contamination of mycoplasma was not detected in those cells using PlasmoTest™ Mycoplasma Detection Kit (InvivoGen) at the time of cryopreservation. No cells were passaged for more than two months *in vitro*.

Human Bone Metastasis Samples

The protocols for collection and use of human bone metastasis samples were performed in accordance with the Declaration of Helsinki and approved by Institutional Review Board at Baylor College of Medicine (H-49396), University of Texas MD Anderson Cancer Center (PA15-0225) and University of Texas Medical Branch (H-46675), respectively. All the patients have provided written informed consent on the use of their samples for research purpose when undergoing the orthopedic surgery.

Animals

The *in vivo* procedures and usage of animal models were conducted in accordance with the protocol (AN-5734) approved by the Baylor College of Medicine Institutional Animal Care and Use Committee. C57BL/6J (B6, stock no. 000664, RRID:IMSR_JAX:000664), BALB/cJ (BALBc,

Downloaded from http://aacrjournals.org/cancerdiscovery/article-pdf/doi/10.1158/2159-8290.CD-22-0220/3217471/cd-22-0220.pdf by Washington University St Louis user on 10 November 2022

stock no. 000651, RRID: IMSR_JAX:000651), B6.Cg-Gt(ROSA)26Sortm14(CAG-tdTomato)Hze/J (B6-tdRED, stock no. 007914, RRID: IMSR_JAX:007914), C57BL/6-Gt(ROSA)26Sortm1(HBEGF)Awai/J (B6-iDTR, stock no. 007900, RRID: IMSR_JAX:007900), B6.Cg-Tg(Cspg4-cre/Esr1*)BAkik/J (NG2-CreERTM, stock no. 008538, RRID: IMSR_JAX: 008538), C57BL/6-Tg(Nes-cre/ERT2)KEisc/J (Nes-cre/ERT2, stock no. 016261, RRID: IMSR_JAX: 016261), B6.129(Cg)-Leprtm2(cre)Rck/J (Lepr-Cre, stock no. 008320, RRID: IMSR_JAX: 008320), B6.Cg-Tg(Tek-cre)1Ywa/J (Tie2-Cre, stock no. 008863, RRID: IMSR_JAX: 008863), B6.129S6(SJL)-Cdh2tm1Glr/J (N-cadflox, stock no. 007611, RRID: IMSR_JAX: 007611) were purchased from Jackson Laboratories. Osteocalcin-GFP (Ocn-GFP, RRID: N/A) strain was kindly provided by Dr. Dongsu Park (BCM). To generate $Cre^{+/-}$;$tdRED^{+/+}$ reporter strains, the male Cre^{+} transgenic mice were breed with female $tdRED^{+/+}$ for two rounds to generate a Cre positive strain with homozygous tdRED insertions. Then the male $Cre^{+/-}$;$tdRED^{+/+}$ reporter mice were mated with female $iDTR^{+/+}$ mice to generate $Cre^{+/-}$;$tdRED^{+/-}$;$iDTR^{-/+}$ mice for lineage depletion models. For the *in vivo* tracing of osteogenic differentiation, the male NG2-$CreERTM^{+/-}$;$tdRED^{+/+}$ strain was crossed with female Ocn-$GFP^{+/-}$ strain to generate NG2-$CreERTM^{+/-}$;$tdRED^{+/-}$;Ocn-$GFP^{+/-}$ strain. For N-cadherin knockout model, the male NG2-$CreERTM^{+/-}$;$tdRED^{+/+}$ strain was crossed with female N-$cad^{flox/flox}$ strain for two rounds to generate NG2-$CreERTM^{+/-}$;N-$cad^{flox/flox}$;$tdRED^{+/-}$ or NG2-$CreERTM^{+/-}$;N-$cad^{flox/flox}$;$tdRED^{-/-}$ mice. B6.NG2-CreERTM and B6.tdRED mice were backcrossed to BALB/cJ for more than ten generations in our lab and then crossed to breed BALBc. NG2-$CreERTM^{+/-}$;$tdRED^{+/+}$ strain.

PCR Genotyping

Genomic DNA of ear tissues was purified by MasterPure™ DNA Purification Kit (Epicentre, MC85200). PCR primers for genotyping of Cre allele were: Cre-F, 5'-GCG GTC TGG CAG TAA AAA CTA TC-3'; Cre-R, 5'-GTG AAA CAG CAT TGC TGT CAC TT-3'. Primers for genotyping of Rosa26-tdRED allele were: tdRED-F, 5'-GGC ATT AAA GCA GCG TAT CC-3'; tdRED-R, 5'-CTG TTC CTG TAC GGC ATG G-3'; tRED-WT-F, 5'-AAG GGA GCT GCA GTG GAG TA-3'; tRED-WT-R, 5'-CCG AAA ATC TGT GGG AAG TC-3'. Primers for genotyping of Rosa26-iDTR allele were: iDTR-Com, 5'-AAA GTC GCT CTG AGT TGT TAT-3'; iDTR-R, 5'-GCG AAG AGT TTG TCC TCA ACC-3'; iDTR-WT-R, 5'-GGA GCG GGA GAA ATG GAT ATG-3'. Primers for genotyping N-$cad^{flox/flox}$ allele were: CDH2 KO-F, 5'-CCA AAG CTG AGT GTG ACT TG-3'; CDH2 KO-R, 5'-TAC AAG TTT GGG TGA CAA GC-3'. Primers for Ocn-GFP genotyping were: GFP-F, 5'-CTG GTC GAG CTG GAC GGC GAC GTA AC-3'; GFP-R, 5'-ATT GAT CGC GCT TCT CGT TGG GG-3'.

Downloaded from http://aacrjournals.org/cancerdiscovery/article-pdf/doi/10.1158/2159-8290.CD-22-0220/3217471/cd-22-0220.pdf by Washington University St Louis user on 10 November 2022

Induction of Cre-mediated recombination and depletion of Cre-expressing lineages

If not specified otherwise, all the *in vivo* experiments were performed using female mice and the $Cre^{-/-}$ littermates were used as age-matched controls. To induce CreER activity, 5-week-old female mice were injected with 1mg tamoxifen (Sigma) daily for 5 consecutive days (for lineage tracing experiment and isolation of BMSCs) or two cycles of 5 consecutive days with a 2-day interval (for in vivo experiments). To deplete the Cre-expressing lineage, mice were intraperitoneally injected with 200 ng Diphtheria Toxin (DT, 20ng for Tie2-Cre) (Sigma-Aldrich, D0564) for 3 consecutive days in every 10-day cycle.

Subcutaneous Implantation and Tumor Removal Surgery

All the animal surgeries were performed using aseptic procedures and started with 7-8 weeks old animals except for Figure 2B (due to the institutional lockdown during pandemic, this batch of experiments were started with about 3-month-old animals). If not specified, 20E4 LLC1 Fluc-EGFP cells were mixed with equal volume of growth factor reduced Matrigel matrix (Corning, Cat# 356231,or R&D Systems, Cat# 3433-010-01) and subcutaneously injected into the skin close to the right hindlimb. The tumors took about 18 days to reach 1.2 cm in diameter, and a tumor removal surgery was performed to completely remove the primary tumors. About 20% of subjects met the criteria of early euthanasia before day 32 due to lung metastasis and were not included in final analysis. Most animals survived about five weeks after the implantation of primary tumors, and were dissected and examined at day 32-35 for lung and bone metastasis.

Femoral Bone Fracture Repairing Models

For the drill-hole model, a 7-mm-long posterior skin incision was made along the fumural bones. Then the muscle was carefully displaced to expose the femur shaft and a defect was created on the central femoral bones by a 0.7-mm-diameter drill bit with the electric drill (Dremel 8050-N/18 Micro). For the bending model, an about 1-cm-long incision was made over the anterior skin from the knee to the proximal femur. To stabilize the fractured femurs, a sterile, 0.2 mm diameter minutien stainless steel pin (Fine Science Tools, cat #26002-20) was inserted into the bone marrow cavity from the femoral plateau. The fracture was then created by 3-point bending. To facilitate the following bone sectioning, the steel pins were removed by another survival surgery 1 week later. For both models, the skin wound was closed with tissue glue and wound clips and mice were given post-operative analgesia for 6 days and monitored twice daily. If not specified, the wounded bones were collected about 17 days after the fracture surgeries.

Intraosseous Implantation of Tumor Cells or BMSCs

Downloaded from http://aacrjournals.org/cancerdiscovery/article-pdf/doi/10.1158/2159-8290.CD-22-0220/3217471/cd-22-0220.pdf by Washington University St Louis user on 10 November 2022

To directly implant tumor cells in the wounded bone areas, the same 0.7-mm-diameter drill bit was used to carefully thin the femoral shaft without touching the bone marrow cavity. Then, 10 ul of tumor cell suspension with extracellular matrix was injected by a 28G insulin syringe (Becton Dickinson, Cat# 329461) through the thinned region. For the transplantation of BMSCs into the bone, a skin open was made on the knee region and the syringe was slowly inserted into the femoral cavity through the metaphyseal cartilage. The injection created an about 0.4-mm-diameter bone defect. Then, a new syringe with BMSCs were inserted along the hole into the bone marrow cavity and BMSCs were slowly injected. Syringes were held in place for 1 minute to allow the pressure to equilibrate and avoid leakage of cell suspension.

Intra-Iliac Artery Injection

Intra-iliac artery injection of tumor cells was performed as previously described(12,30). Briefly, animals were given pre-operative analgesia, anesthetized and positioned on a warming pad. The surgical area was cleaned and sterilized and a 7-8 mm incision was made between the fourth and the fifth nipples. The iliac artery was carefully exposed by removing the adjacent tissues. 5E4 tumor cells were suspended in 100µl PBS and slowly injected to the iliac artery by 31G insulin syringe (Becton Dickinson, Cat# 328418). After the equilibration of blood flow, the syringe was retrieved and cotton tips were gently applied to the surgical area to stop the bleeding before wound was closed.

Bioluminescence Imaging and Quantification

For the IIA model and intra-osseous implantation model, the *in vivo* bioluminescent imaging was performed with IVIS Lumina II (Perkin Elmer) at the indicated time points. Briefly, the hair on the posterior side of injected hindlimb was removed to allow the penetration of bioluminescence before animals were given with 100 µl 15 mg/ml D-luciferin (Gold Biotechnology, Cat# LUCK-5G) via retro-orbital injection. For the spontaneous metastasis model, to eliminate the influence of remaining or recurred primary tumors, only the *ex vivo* BLI imaging on the dissected tissues was performed. Animals were scanned immediately at D mode right after administration of luciferin. The exposure time was manually adjusted between 1-120 seconds to avoid signal saturation. To quantify the total BLI intensity of a specified tissue, a fixed region of interest was apply to all animals or dissected tissues and the total bioluminescent counts were quantified. The values were then normalized to exposure time to ease the comparison between batches of scanning with different exposure lengths. The presence of metastases on the specific organ was defined as the detection of clustered BLI signals above 15 counts/pixel under a maximum 120-second exposure. To quantify the distribution of BLI signals along the femoral bones, the BLI

Downloaded from http://aacrjournals.org/cancerdiscovery/article-pdf/doi/10.1158/2159-8290.CD-22-0220/3217471/cd-22-0220.pdf by Washington University St Louis user on 10 November 2022

images were exported as 8-bit Grey graphs with log10 transformed BLI spectrum ranging from 15 to 65535 count/pixel. Then, a rectangle ROI with 100 pixels(length)X30 pixels (width) was draw from the distal end to the proximal end of femoral bones. The distribution of transformed BLI intensities along this ROI was measured by the 'Plot Profile' function of ImageJ.

Tissue Collection and Bone Sectioning

To collect tissues for immunostaining, animals were pre-perfused with 30 ml 10 IU/ml heparin PBS solution to completely remove the blood cells before dissection. The dissected tissues were then fixed overnight in 4% PFA. Bone tissues were decalcified with 0.5M PH7.4 EDTA solution overnight except those for bone histomorphometry assay and new bone formation assay. Then, tissues were cryopreserved in 30% sucrose PBS solution and embedded in OCT. CryoJane tape-transfer system (Leica) was used to collect high-quality 10 μm thick sections from frozen bone tissues. The frozen sections were kept in -80℃ freezer until further staining. The Breast Center Pathology Core at Baylor College of Medicine assisted with the preparation and sectioning of paraffin embedded tissues and cells.

Bone Formation Rate

To determine the rate of new bone formation, animals were pretreated with tamoxifen to induce CreER activity at age of 5 weeks and later subjected to two rounds of DT treatment from week 7 if needed. On week 10, mice were injected with 20mg/kg Calcein dissolved in 2% sodium bicarbonate solution (4mg/ml stock solution) (Sigma, Cat# C0875-5G) via retro-orbital venous. 5 days later, mice were given with another dose of 40mg/kg Alizarin Red S (Acros Organics, Cat# AC400480250) in PBS (8mg/ml stock solution) through retro-orbital injection. On day 7, the mice were euthanized, perfused and dissected. Hindlimb bones were collected, fixed and embedded immediately in OCT. The non-decalcified bone were sectioned by a Leica CM3050S Cryostat installed with CryoJane tape-transfer system with low profile microtome blades. Bone sections were then mounted with Prolong™ Gold Antifade Mountant with DPAI (Invitrogen, Cat# P36935) and three different parts of each femur bone were randomly imaged by confocal microscope. The distance between Calcein and Alizarin Red S positive bands were calculated by Zen software (Zeiss).

Bone Histomorphometry

For bone histomorphometry analysis, mice from the same litter were treated with tamoxifen to induce Cre activity and later subjected to two rounds of DT treatments. Femur bones were collected 3 weeks later, fixed in 4% PFA overnight, and transferred to the Research Histology

Downloaded from http://aacrjournals.org/cancerdiscovery/article-pdf/doi/10.1158/2159-8290.CD-22-0220/3217471/cd-22-0220.pdf by Washington University St Louis user on 10 November 2022

Core at UT MD Anderson Cancer Center in 70% ethanol PBS. There, bone samples were embedded and sectioned in methylmethacrylate block. The Goldner's Trichrome and TRAP enzymatic staining were performed by Bone Histomorphometry Core at UT MD Anderson Cancer Center and analyzed by Leah Guerra (UT MDACC).

microCT Analysis of Bone Samples

Femur bones were dissected, cleaned, fixed in 70% ethanol PBS solution, and scanned by a Bruker Skyscan 1272 scanner (Bruker-MicroCT) at 50 kVp, 200 μA X-ray energy. The image resolution was 6 μm. 0.60° rotation angle and averaging of three scannings were applied at each step for a total 360° rotation. Three-dimensional bone images were reconstructed by CTvox (Bruker-MicroCT, v3.0.0) and the cross sectional images were generated by NRecon (Bruker-MicroCT, v1.6.9.8) and DataViewer (Bruker-MicroCT, v1.5.6.2). To quantify new bone formation after fracture surgery, a fixed ROI was applied to extract same volume of cortical bone around the defect area with minimal adjacent non-wounded bone tissue. Specifically, for drill-hole experiments, a circle ROI was draw on the 200 axial cortical bone slides around the drill site, while for the intra-growth plate transplantation of BMSCs, a rectangular area with 50 coronal trabecular bone slides below the damaged growth plate was chosen for further analysis. Bone volume were then analyzed via CT Analyzer (Bruker-MicroCT, v1.15.4.0).

Immunofluorescent Staining on Bone Sections

For paraffin embedded sections, slides were baked at 55℃ overnight, dewaxed, and rehydrated using the standard protocol. Antigen retrieval was performed using a pressure cooker at 125℃, 25 psi for 5 minutes with PH9.0 EDTA-Tris solution. For frozen sections, the slides were taken out of the freezer and warmed at room temperature for 10 minutes before rinsed by PBS. All the slides were treated with 0.1M NH_4Cl solution for 10 minutes to reduce the autofluorescence and blocked in 10% donkey serum in PBS-GT (2% Gelatin, 0.5% TritonX-100) for 1 hour at RT. If the mouse primary antibodies were used on mouse tissues, M.O.M. Blocking Reagent (Vector Laboratories) were used for additional blocking. The slides were then incubated with primary antibodies at 4℃ overnight and then stained with corresponding secondary antibodies for 2 hours. The primary antibodies used in this study include: Chicken anti-GFP (Abcam, Cat# ab13970, RRID: AB_300798, 10mg/ml, 1:500); Rabbit anti-mRFP (Rockland, Cat# 600-401-379, RRID: AB_2209751, 1mg/ml, 1:500); Goat anti-mouse VE-Cadherin (R&D system, Cat# AF1002, RRID: AB_2077789; 1mg/ml, 1:200); Goat anti-mouse CD31(R&D system, Cat# AF3628, RRID: AB_2161028, 1mg/ml, 1:200); Rat anti-mouse Endomucin (Santa Cruz, Cat# sc-65495, RRID: AB_2100037, 200μg/ml, 1:100); Rabbit anti-mouse Ki67 (Abcam, Cat# ab15580,

Downloaded from http://aacrjournals.org/cancerdiscovery/article-pdf/doi/10.1158/2159-8290.CD-22-0220/3217471/cd-22-0220.pdf by Washington University St Louis user on 10 November 2022

RRID: AB_443209, 1mg/ml, 1:100, for frozen sections); Rat anti-mouse Ki67 (eBioscience, Cat# 14-5698-82, RRID: AB_10854564, 0.5mg/ml, 1:100, for paraffin embedded sections); Rabbit anti-mouse NG2 (EMD Millipore, Cat# AB5320, RRID: AB_11213678, 1mg/ml, 1:200); Goat anti-mouse Leptin Receptor (R&D system, Cat# AF497, RRID: AB_2281270, 1mg/ml, 1:100); Rabbit anti-mouse PDGFRβ (Abcam, Cat# ab32570, RRID: AB_7771650.162mg/ml, 1:100); Rabbit anti-mouse Aggrecan (Millipore Sigma, Cat# AB1031, RRID: AB_90460, 0.5mg/ml, 1:100); Rabbit anti-mouse Perilipin A/B (Sigma, Cat# P1873, RRID: AB_532267, 1.0~1.4mg/ml, 1:100); Rabbit anti-human NG2 (Cell Signaling Technology, Cat# 43916S, RRID: N/A , 18μg/ml, 1:50); Mouse anti-human/mouse N-Cadherin (BD Bioscience, Cat# 610921, RRID: AB_398236, 250μg/ml, 1:25); Mouse anti-human/mouse N-Cadherin (Invitrogen, Cat# 33-3900, RRID: AB_2313779, 0.5mg/ml, 1:25);Rat anti-human cytokeratin-8 (DSHB, Cat# TROMA-I, RRID: AB_531826, 1:200); Rat anti-human cytokeratin-19 (DSHB, Cat# TROMA-III, RRID: AB_2133570, 1:200); Mouse anti-DsRed Alexa Fluor 594 (Santa Cruz, Cat# sc-390909 AF594, RRID:AB_2801575, 200μg/ml, 1:100); Rabbit anti-Osteocalcin (Abcam, Cat# ab93876, RRID:AB_10675660, 1mg/ml, 1:100); Rabbit anti-S6K1 (phospho T389+T412) (Abcam, Cat# ab60948, RRID:AB_944606, 1mg/ml, 1:100); Goat anti-mouse E-Cadherin (R&D system, Cat# AF748, RRID:AB_355568, 0.2mg/ml, 1:50). The secondary antibodies used in this study include: Donkey anti-chicken Alexa Fluor 488 (Jackson ImmunoResearch, Cat# 703-545-155, RRID: AB_2340375, 2mg/ml, 1:500); Donkey anti-mouse Alexa Fluor 488 (Jackson ImmunoResearch, Cat# 715-545-151, RRID: AB_2341099, 2mg/ml, 1:500); Donkey anti-rabbit Alexa Fluor 488 (Jackson ImmunoResearch, Cat# 711-546-152, RRID:AB_2340619, 2mg/ml, 1:500); Donkey anti-goat Alexa Fluor 488 (Jackson ImmunoResearch, Cat# 705-546-147, RRID:AB_2340430, 2mg/ml, 1:500);Donkey anti-rabbit Alexa Fluor 555 (Invitrogen, Cat# A-31572, RRID: AB_162543, 2mg/ml, 1:500); Donkey anti-rat Brilliant Violet 480 (Jackson ImmunoResearch, Cat# 712-685-153, RRID: AB_2651113, 1:200); Donkey anti-rat Alexa Fluor 555 (Abcam, Cat# ab150154, RRID:AB_2813834, 2mg/ml, 1:500); Donkey anti-rat Alexa Fluor 647 (Jackson ImmunoResearch, Cat# 712-605-153, RRID: AB_2340694, 2mg/ml, 1:500); Donkey anti-goat Alexa Fluor 555 (Invitrogen, Cat# A-21432, RRID:AB_2535853, 2mg/ml, 1:500); Donkey anti-chicken Alexa Fluor 647 (Jackson ImmunoResearch, Cat# 703-606-155, RRID:AB_2340380, 2mg/ml, 1:500); Donkey anti-goat Alexa Fluor 647 (Jackson ImmunoResearch, Cat# 705-605-147, RRID: AB_2340437, 2mg/ml, 1:500); Donkey anti-rabbit Brilliant Violet 421 (Jackson ImmunoResearch, Cat# 711-675-152, RRID: AB_2651108, 1:100). TROMA-I and TROMA-III were deposited to the DSHB by Brulet, P. / Kemler, R. (DSHB Hybridoma Product TROMA-I/ TROMA-III). The tdTomato protein maintains fluorescent activity

Downloaded from http://aacrjournals.org/cancerdiscovery/article-pdf/doi/10.1158/2159-8290.CD-22-0220/3217471/cd-22-0220.pdf by Washington University St Louis user on 10 November 2022

in PFA fixed frozen tissues and therefore does not require additional staining if other rabbit derived primary antibodies have to be used on the same slides. Whenever compatible, Hoechst 33342 (Thermo Fisher Scientific, Cat# 62249, 1μg/ml) was used for nucleus staining. The stained slides were mounted with Prolong™ Gold Antifade Mountant (Invitrogen, Cat# P36934) and scanned by either a Zeiss LSM880 confocal microscope or a Zeiss AxioScan.Z1 slide scanner. To acquire images of large field, the tile scanning was performed with 5% overlap. The fluorescent images were exported as tif format by Zen software and further analyzed by ImageJ. Briefly, the threshold was re-adjusted to filter the background and increase the brightness for each channel. Despeckle function of ImageJ was applied to the images to reduce the noise. To quantify the expression of phosphorylated S6K1 in tumor cells, the GFP^+ area were segmented and the mean cytoplasmic intensity of pS6K1 was quantified by CellProfiler (Broad Institute, v4.1.3) (60).

Whole-mount Staining and Bone Clearing

The OCT-embedded, intact hindlimbs were sectioned on both sides by cryostat to expose bone marrow cavity and become about 500μm thick sections. The sections were then rinsed by PBS to completely remove embedding material and incubated with 1mg/ml Sodium Borohydride solution for 30 minutes to reduce the autofluorescence. Samples were then transferred into a 1.5 ml Eppendorf tube with 1ml blocking buffer (10% DMSO, 5% donkey serum, 0.5% IGEPAL-CA630, 1% anti-mouse CD16/32 Fc-Blocking antibody(Tonbo Bio, 70-0161-M001), 1% BlokHen (Aves Labs)), and rotated in 4℃ overnight. The second day, samples were stained with primary antibodies in 10% DMSO, 5% donkey serum, 0.5% IGEPAL-CA630 staining buffer, including Chicken anti-GFP (Abcam, Cat# ab13970, RRID:AB_300798, 10mg/ml, 1:100), Rabbit anti-mRFP (Rockland, Cat# 600-401-379, RRID:AB_2209751, 1mg/ml, 1:100), Goat anti-mouse VE-Cadherin (R&D system, Cat# AF1002, RRID:AB_2077789, 1mg/ml, 1:100), Goat anti-mouse CD31(R&D system, Cat# AF3628, RRID:AB_2161028, 1mg/ml, 1:100), for three days in 4℃ with constant rotation. After several times of PBS washing for one day, samples were stained with donkey anti-chicken Alexa Fluor 488 (Jackson ImmunoResearch, Cat# 703-546-155, RRID: AB_2340376, 2mg/ml, 1:100), donkey anti-rabbit Alexa Fluor 555 (Invitrogen, Cat# A-31572, RRID: AB_162543, 2mg/ml, 1:100), donkey anti-goat Alexa Fluor 647 (Jackson ImmunoResearch, Cat# 705-606-147, RRID: AB_2340438, 2mg/ml, 1:100) in staining buffer for three days in 4℃ with rotation. After one-day PBS washing, samples were sequentially dehydrated in 30%, 50%, 70%, 90%, 100% and 100% methanol per hour and then incubated with 100% methanol overnight. After dehydration, bone samples were transferred to 5ml

Downloaded from http://aacrjournals.org/cancerdiscovery/article-pdf/doi/10.1158/2159-8290.CD-22-0220/3217471/cd-22-0220.pdf by Washington University St Louis user on 10 November 2022

Eppendorf tube with fresh BABB clearing reagent (1:2 Benzoic Acid:Benzyl Benzoate) and incubated at room temperature with gentle shaking for 2 days. The cleared bone samples were later mounted with BABB in a customized glass cassette with depth adjustable spacer (Sunjin Lab, Cat# IS002). The deep imaging was performed immediately with an Olympus FV1200 MPE confocal microscope. Specifically, a 10X water immersed objective with 8mm working distance was used to obtain high resolution three dimensional image stacks. Meanwhile, the laser power and PMT gain were scaled on different depths to generate images with uniform intensity. The mosaic scanning of whole bone area was achieved with the motorized XY stage. The images were then stitched and exported as 8-bit tiffs by Fluoview (Olympus), and the whole-view projection images were created by ImarisViewer (Oxford Instruments, v9.5.1).

Spatial Analysis of Tumor Cells in Bone

The spatial distribution of tumor cells relative to NG2-tdRED+ cells or bone marrow vasculature was performed with a customized pipeline by MATLAB (MathWorks, v9.6). Basically, the region of interest (bone marrow canal hereafter) were manually chosen from each image slide to remove the exterior periosteum and connective tissues, which typically contain saturated signals. Geometric active contour (GAC) was used to segment the cells and vessels from original images. GAC is a form of contour model that adjusts the smooth curve established in the Euclidean plan by moving the curve's points perpendicularly. The points move at a rate proportionate to the curvature of the image's region. The geometric flow of the curve, which encompasses both internal and external geometric measures in the region of interest, and the recognition of items in the image were used to characterize contours. In the process of detecting items in an image, a geometric replacement for snakes was utilized. For segmentation of tumor cells, a threshold of 50 μm^2 in 2D images or 100 voxels for 3D images was set to remove the cell debris or false positive signals. For the analysis of 2D fracture bone images, the new bones were manually labelled based on the presence of $Hoechst^+GFP^-Endomucin^-Ki67^-$ osteocytes. After the segmentation, a matrix with the spatial positions of cancer cells (with or without Ki67 status), blood vessels, and $NG2\text{-}tdRED^+$ cells was created and further analyzed. For random spots simulation, 1000 spots with 10 μm diameter were randomly inserted in the image stacks after filtering the intravascular and bone matrix space and their distances to the closest target were computed as described above.

Isolation of Whole Bone Cells

A customized protocol was used in the lab to collect cells from both bone marrow cavity and endosteal compartments of bones. Fresh long bones were dissected immediately from the

Downloaded from http://aacrjournals.org/cancerdiscovery/article-pdf/doi/10.1158/2159-8290.CD-22-0220/3217471/cd-22-0220.pdf by Washington University St Louis user on 10 November 2022

euthanized animals and placed in 24-well plate containing 2 ml PBS with 2% FBS. The muscle and connective tissues were then carefully removed, and the hindlimb was broke off from the joint area to separate the femur and tibia bones. Bones were then transferred to a new well with 2% FBS PBS, and both metaphyseal ends were cut off to expose the bone marrow canal. For the quantification of cells at the fracture areas, both ends of femur bones were cut off and only the central shaft bones were subjected to the following procedures. Bone marrow was flushed out by 26G syringe with 2% FBS PBS into the wells and bone marrow cavity was thoroughly washed until the bones became pale. Bone marrow plugs were gently aspirated to become single cell suspension in red blood cell (RBC) lysis buffer (Tonbo Biosciences, Cat# TNB-4300-L100). The remaining bones were moved to 12-well plate and excised into 1-2mm bone chips by scissors. To release bone attaching cells, fragmented bones were digested with 2 ml DMEM medium containing 1 mg/ml Collagenase I (Sigma, Cat# C0130), 1 mg/ml Collagenase II (Thermo Fisher Scientific, Cat# 17101015), 4 mg/ml Dispase II (Sigma, Cat# D4693), 1 mg/ml BSA, 0.1 mg/ml DNase I (Sigma, Cat# DN25), 10 mM HEPES, 1mM EDTA in 37°C, 5% CO2 for 45 minutes. The digested bones were then washed with 10 ml 10% FBS PBS and then PBS. The released cells from enzyme digestion and PBS washing were pooled and centrifuged. The endosteum derived cells and the bone marrow cells can then be processed separately (Figure S3A) or combined (others) for flow cytometry. To enable the detection of rare tumor cells in bones 1 day post IIA injection (Figure S2Q-S), the released bone cells were subjected to MACS sorting to deplete the majority of immune cells before flow cytometry.

Flow Cytometry

The bone cell suspension was firstly pass through 70 μm cell strainer to completely remove bone debris and aggregated cells, and then re-suspended in 10 ml RBC lysis buffer to get rid of most blood cells. After 10 minute incubation at room temperature, cells were centrifuged and re-suspended with 1 ml 2% FBS PBS. Samples were then aliquoted for staining of different panels (250μl per panel) and blocked with anti-CD16/32 antibody (Tonbo, Cat# 40-0161, RRID: AB_2621443, 0.2mg/ml, 1:100) for 10 minutes on ice, followed by staining of fluorescent dye-conjugated primary antibodies or istotype control antibodies on ice for 20 minutes. The antibodies used in this study include: immune cells panel, CD45-VF450 (Tonbo, Cat# 75-0451, RRID: AB_2621947, 0.2mg/ml, 1:200), CD11b-APC/Cy7 (Tonbo, Cat# 25-0112, RRID: AB_2621625, 0.2mg/ml, 1:200), Ly6G-Percp/Cy5.5 (Tonbo, Cat# 65-1276, RRID: AB_2621899, 0.2mg/ml, 1:200), Ly6C-PE/Cy7 (BioLegend, Cat# 128018, RRID: AB_1732082, 0.2mg/ml, 1:200), CD3e-PE (Tonbo, Cat# 50-0031, RRID: AB_2621730, 0.2mg/ml, 1:200), CD4-APC

Downloaded from http://aacrjournals.org/cancerdiscovery/article-pdf/doi/10.1158/2159-8290.CD-22-0220/3217471/cd-22-0220.pdf by Washington University St Louis user on 10 November 2022

(Tonbo, Cat# 20-0041, RRID: AB_2621543, 0.2mg/ml, 1:200), CD8a-FITC (Tonbo, Cat# 35-0081, RRID: AB_2621671, 0.5mg/ml, 1:200), F4/80-BV605 (BioLegend, Cat# 123133, RRID: AB_2562305, 0.1mg/ml, 1:200) and B220-BV711 (BioLegend, Cat# 103255, RRID: AB_2563491, 0.2mg/ml, 1:200); stromal cell panel, CD45-BV605 (BioLegend, Cat# 103140, RRID: AB_2562342, 0.2mg/ml, 1:200), Ter119-VF450 (Tonbo, Cat# 75-5921, RRID: AB_2621967, 0.2mg/ml, 1:200), CD31-AF647 (BioLegend, Cat# 102506, RRID: AB_312913, 0.5mg/ml, 1:200), Sca-1-Percp/Cy5.5 (eBioscience, Cat# 45-5981-82, RRID: AB_914372, 0.2mg/ml, 1:200), CD51-PE (BioLegend, Cat# 104106, RRID: AB_2129493, 0.2mg/ml, 1:200), CD140α-PE/Cy7 (BioLegend, Cat# 135912, RRID: AB_2715974, 0.2mg/ml, 1:200); Treg and Ki67 panel, CD45-VF450 (Tonbo, Cat# 75-0451, RRID: AB_2621947, 0.2mg/ml, 1:200), CD3e-Percp/Cy5.5 (Tonbo, Cat# 65-0031, RRID: AB_2621872, 0.2mg/ml, 1:200), CD4-PE/Cy7 (Tonbo, Cat# 60-0041, RRID: AB_2621828, 0.2mg/ml, 1:200), CD8a-BV711 (BioLegend, Cat# 100759, RRID: AB_2563510, 0.2mg/ml, 1:200), Foxp3-PE (Tonbo, Cat# 50-5773, RRID: AB_2621797, 0.2mg/ml, 1:200), and Ki67-APC (BioLegend, Cat# 652406, RRID: AB_2561930, 0.2mg/ml, 1:200); Apoptotic cells, Annexin V-APC/7-AAD Kit (Tonbo, Cat# 20-6410-KIT, 5μl for Annexin V, 025μg 7-AAD). The staining of nuclear proteins Foxp3 and Ki67 was performed with Foxp3/Transcription Factor Fixation/Permeabilization kit (eBioscience, Cat# 00-5521-00). After the staining, the live cells were re-suspended in 200μl FACS buffer with a drop of DAPI (Invitrogen, Cat# R37606). To quantify the absolute number of tumor cells per bone sample, a determined amount of counting beads (BD Bioscience, Cat# 335925) was added. The absolute number was calculated as (gated events)/(gated counting bead events)*10*250(μl)*4. The flow cytometry was run on a BD LSRFortessa flow cytometer and further analyzed by FlowJo software (BD, v10.7.1). The markers for gating each population were: B cells, $DAPI^-CD45^+CD11b^-B220^+$; T cells, $DAPI^-CD45^+CD11b^-CD3e^+$; CD4 T cells, $DAPI^-CD45^+CD11b^-CD3e^+CD4^+$; CD8 T cells, $DAPI^-CD45^+CD11b^-CD3e^+CD8a^+$; $Ly6C^{hi}$ Monocytes, $DAPI^-CD45^+CD11b^+Ly6C^+Ly6G^-$; Neutrophils, $DAPI^-CD45^+CD11b^+Ly6C^+Ly6G^+$; $Ly6C^{lo}$ Monocytes, $DAPI^-CD45^+CD11b^+Ly6C^{low/-}Ly6G^-$; Macrophages, $DAPI^-CD45^+CD11b^+Ly6C^-Ly6G^-F4/80^+$; Treg cells, $CD45^+CD3e^+CD4^+CD8^-Foxp3^+$; Tumor cells, $DAPI^-CD45^-GFP^+$; $tdRED^+$ BMSCs, $DAPI^-CD45^-Ter119^-CD31^-tdRED^+$; Tie2-$tdRED^+$ cells, $DAPI^-CD45^-Ter119^-tdRED^+$; $PDGFR\alpha^+$, $CD51^+$, or $Sca\text{-}1^+$ BMSCs, $DAPI^-CD45^-Ter119^-CD31^-PDGFR\alpha^+$(or $CD51^+$, $Sca\text{-}1^+$). The exact gating strategies were summarized in Supplementary Figure 1.

Transplantation of bone mesenchymal stromal cells

Downloaded from http://aacrjournals.org/cancerdiscovery/article-pdf/doi/10.1158/2159-8290.CD-22-0220/3217471/cd-22-0220.pdf by Washington University St Louis user on 10 November 2022

To isolate enough number of $NG2^+$ bone mesenchymal stromal cells for transplantation, the whole bone cells were prepared and pooled from the bones (femur, tibia, calvarium, sternum bones) of nine NG2-$CreERTM^{+/-}$;$tdRED^{+/+}$ female mice. To facilitate cell sorting, the majority of immune cells were pre-depleted by MACS sorting. Briefly, whole bone cells were incubated with CD45-biotin, CD11b-biotin, CD3e-biotin, Ly-6C/G-biotin and TER-119-biotin (BD Bioscience, Cat# 559971) in PBS with 2% serum, 1% antibiotics for 15 minutes at 4°C. After washing, cells were re-suspended and incubated with Streptavidin-bound magnetic beads (BD Bioscience, Cat# 557812) for 15 minutes at 4°C. Then cells were rinse twice and the biotin negative cells were collected by EasySep™ Magnet (StemCell, Cat# 18000). The $CD45^-CD31^-TER119^-DAPI^-$ NG2-$tdRED^+$ cells were immediately sorted from the enriched population by a BD Aria II cell sorter with 100 μm nozzle. About 120000 cells in total were collected and then re-suspended in 60μl PBS. Purified cells were directly transplanted into the femur bones of five 8-week-old female C57BL/6 mice (10μl per animal) through intra-femoral injection with a 28G BD insulin syringe. As sham controls, 5 age-matched female C57BL/6 mice were injected with 10μl PBS.

Isolation and *In vitro* Culture of Bone Mesenchymal Stromal Cells

The isolation and *in vitro* expansion of bone derived mesenchymal stromal cells was performed as previously described (61) in a aseptic environment. Briefly, 3-week-old female NG2-$CreERTM^{+/-}$;$tdRED^{+/+}$ mice were treated with tamoxifen for three days to induce Cre activity and tdRED expression in NG2+ cells. One week later, the mice were euthanized and immediately immersed in 70% ethanol for 3 minutes. Hindlimb bones were dissected using sterile scissors and forceps, and the attached tissues were carefully rub away with autoclaved tissue papers. Femurs and tibias were then disconnected from the joint and placed in a sterile cell culture dish with 10 ml α-MEM supplemented with 2% FBS and antibiotics. Bone canals were exposed by cutting off both ends of the marrow cavity and the bone marrow was flushed away with the medium by 26G syringe. The cleaned bones were then transferred to a 35 mm cell culture dish, crashed and fragmented into 1-2mm chips with sterile bone pliers and scissors, and digested with 3 ml α-MEM medium containing 1mg/ml Collagenase II (Thermo Fisher Scientific, Cat# 17101015), 10% FBS and antibiotics at 37°C on a shaker with 200 r.p.m for 1 hour. The digested bones were then collected, rinsed by α-MEM medium, and placed into a 10 cm culture dish with 10 ml α-MEM medium supplemented with 10% mesenchymal stem cell-qualified FBS (Gibco, Cat# 12662029) and 1% antibiotics. On the second culture day, the medium was changed to remove the floating cells and later the medium was changed every three days. After 7 day in culture, the attached cells were released by digestion of 2 ml MSC specialized

Downloaded from http://aacrjournals.org/cancerdiscovery/article-pdf/doi/10.1158/2159-8290.CD-22-0220/3217471/cd-22-0220.pdf by Washington University St Louis user on 10 November 2022

Trypsin/EDTA (Lonza, Cat# CC-3232) for 3 minutes at 37°C. The detached stromal cells were collected, filtered and washed through the cell strainer. Cells were re-suspended with 0.4ml FACS buffer and then sorted by a BD Aria II cell sorter with a 100 μm nozzle. The $tdRED^+$ and $tdRED^-$ cells were cultured in α-MEM medium supplemented with 10% mesenchymal stem cell-qualified FBS, passaged every week and used within 5 passages after isolation.

CFU-F assay

The CFU-F assay was performed by seeding 2000 NG2-$tdRED^+$ or control NG2-$tdRED^-$ BMSCs in 6-well plate. The cells were then maintained in α-MEM medium with 10% FBS at 37°C, 5%CO_2. 7 days later, the plates were washed twice by PBS and briefly fixed by 10% formalin solution at room temperature for 10 minutes. After fixation, cells were stained with 0.5% crystal violet solution (Sigma, Cat# C0775) for 15 minutes and rinsed by distilled water to remove the unbound dye. After drying, the plates were scanned by Cytation 5 (Biotek) and colonies with more than 50 cells were counted.

***In vitro* Trio-lineage Differentiation assay and Alkaline Phosphatase staining**

For the chondrogenic differentiation assay, the isolated mesenchymal stromal cells were suspended in medium at a density of 10^7 cells/ml, and seeded as a 5 μl micromass drop on the bottom of 24-well plate. Cells were allowed to attach to the plate for 2 hours in the cell culture incubator. Then, 1 ml of StemPro™ Chondrogenesis differentiation medium (Invitrogen, Cat# A1007101) was added to each well. Cells were then maintained in 37°C, 5% CO2 for a minimum of 14 days. The differentiation medium was replenished every three days. At the end point, cells were rinsed with PBS for three times and then fixed with 4% PFA for 30 minutes. After PBS washing, the fixed cells were stained with 1% Alcian blue (8GX) solution (Thermo Scientific, Cat# J60122.14) for 30 minutes, rinsed three times with 0.1N HCl to remove unbound dyes and finally rinsed with PBS for three times. For the osteogenic differentiation assay, 4E4 cells were plated in each well of 96-well plate, and the osteogenic differentiation was induced by StemPro™ Osteogenic differentiation Kit (Invitrogen, Cat# A1007201) for three weeks. The differentiation medium was changed every three days. Then, after 10 minutes fixation by 10% Formalin, cells were stained with fresh 2% Alizarin Red S Solution (Thermo Scientific, Cat# 400480250) at room temperature in the dark for about 45 minutes. The stained plates were then rinsed in distilled water to completely remove unbound dyes. For the adipogenic differentiation assay, 4E4 cells were seeded in 96-well plate with α-MEM complete growth medium supplemented with 2 μM Rosiglitazone (AdipoGen, Cat# AGCR13570M010), 500 μM IBMX (Millipore Sigma, Cat# I5879), 1 μM Dexamethasone (MP Biomedicals, Cat# 0219004025) and

Downloaded from http://aacrjournals.org/cancerdiscovery/article-pdf/doi/10.1158/2159-8290.CD-22-0220/3217471/cd-22-0220.pdf by Washington University St Louis user on 10 November 2022

10 μg/ml insulin (Millipore Sigma, Cat# I9278) for 3 days. Then the differentiated cells were maintained in α-MEM complete growth medium with 10ug/ml insulin for another 2 days. Lastly, cells were briefly fixed by 10% Formalin and rinsed with 60% isopropanol twice. After the plates were complete dried, cells were stained with fresh Oil Red O working solution (Alfa Aesar, Cat# A1298914) for 15 minutes and washed with distilled water to remove excess stain. For the ALP staining, 5E3 BMSCs pretreated with 7-day osteogenic differentiation medium were seeded in each well of 96-well plate. The second day, the cells were briefly fixed and the staining was performed with Alkaline Phosphatase Detection Kit (Millipore Sigma, Cat# SCR004). The images were acquired by a Leica MZ125 stereo-microscope.

mRNA Extraction and qRT-PCR

To isolate the total mRNA, primary mesenchymal stromal cells or cells post 7-day treatment of osteogenesis differentiation medium were trypsinized, collected, washed, and then dissolved in 0.5 ml TRIzol® LS Reagent (Invitrogen, Cat# 10296028). Total mRNA was extracted by Direct-zol RNA miniPrep Kit (Zymo Research, Cat# R2052) with in-column DNase I treatment as instructed by the manufacturer's protocol. 100 ng total RNA was then converted into cDNA using RevertAid First Strand cDNA synthesis Kit (Thermo Scientific, Cat# K1622). Quantitative PCR was carried out with PowerUp SYBR Green Master Mix (Thermo Fisher, Cat# A25743) on a Biorad CFX Real-Time system. The fold changes of mRNA levels were calculated by $2^{-\Delta\Delta Ct}$ with β-actin mRNA level as the internal control. The q-PCR primer sequences used in this study are as follows: *Actb*, 5'-GGCTGTATTCCCCTCCATCG-3', 5'-CCAGTTGGTAACAATGCCATGT-3'; *Pou5f1*, 5'-GGCTTCAGACTTCGCCTTCT-3', 5'-TGGAAGCTTAGCCAGGTTCG-3'; *Sox2*, 5'-AGGAAAGGGTTCTTGCTGGG-3', 5'-GACCACGAAAACGGTCTTGC-3'; *Klf2*, 5'-CACCTAAAGGCGCATCTGCGTA-3', 5'-GTGACCTGTGTGCTTTCGGTAG-3'; *Klf4*, 5'-CTATGCAGGCTGTGGCAAAACC-3', 5'-TTGCGGTAGTGCCTGGTCAGTT-3'; *Pdgfra*, 5'-AAAATGCGGGTTTTGAGCCC-3', 5'-GACCAGAAAGACCTGGTGGG-3'; *Sp7*, 5'-AGCGACCACTTGAGCAAACAT-3', 5'-GCGGCTGATTGGCTTCTTCT-3'; *Cdh2*, 5'-GGGAGGGGTAAAAGTTCTTAGCA-3', 5'-TGGTACACAACACAGACGCA-3'; *Spp1*, 5'-GAGGAAACCAGCCAAGGACTAA-3', 5'-CTGAGATGGGTCAGGCACCA-3'.

Protein Extraction and Western Blotting

For western blotting, the primary mesenchymal stromal cells were directly lysed with RIPA buffer and the total proteins were prepared accordingly. 20 μg of total proteins was loaded in NuPAGE® Novex® Gel system (Invitrogen) and then transferred to the nitrocellulose membrane with iBlot™ Transfer System (Invitrogen). After 1 hour's blocking with 5% milk in TBST buffer,

Downloaded from http://aacrjournals.org/cancerdiscovery/article-pdf/doi/10.1158/2159-8290.CD-22-0220/3217471/cd-22-0220.pdf by Washington University St Louis user on 10 November 2022

membrane was incubated with rabbit anti-mouse N-Cadherin (Abcam, Cat# ab12221, RRID: AB_298943, 1mg/ml, 1:1000) and mouse anti-mouse Gapdh (Santa Cruz, Cat# sc-32233, RRID: AB_627679, 100μg/ml, 1:1000) overnight at 4℃ and stained with corresponding fluorescent secondary antibodies (LI-COR Bioscience, RRID: AB_621843 and RRID: AB_621842) in the second day for 2 hours. The membranes were then scanned by the Odyssey® infrared imaging system.

siRNA transfection

The transfection was performed at about 50% cellular confluency using Lipofectamine™ RNAiMAX (Invitrogen, Cat# 13778075) according to the manufacturer's instruction. Specifically, primary MSCs were transfected with a pooled validated siRNA mixture against mouse N-cadherin (Silencer™ Select siRNAs, Invitrogen, Cat # 4390771-s63770 and s63771) in 15 cm dishes 3 days prior the co-culture assay. For the E-cadherin knock down in tumor cells, murine tumor cells were seeded in 6 well plates and transfected with the pooled siRNA mixture targeting mouse E-cadherin (Silencer™ Select siRNAs, Invitrogen, Cat # 4390771-s63752 and s63753) two days before the co-culture assays. A validated control siRNA (Silencer™ Select siRNAs, Cat # 4390843) was used in parallel as negative controls. The sequence of siRNAs are: siCDH1, s63752, sense, 5"-GAAGAUCACGUAUCGGAUUtt-3', antisense, 5"-AAUCCGAUACGUGAUCUUCtg-3'; siCDH1, s63753, sense, 5"-GACCGGAAGUGACUCGAAAtt-3', antisense, 5"-UUUCGAGUCACUUCCGGUCgg-3'; siCDH2, s63770, sense, 5"-GUGCAACAGUAUACGUUAAtt-3', antisense, 5"-UUAACGUAUACUGUUGCACtt-3'; siCDH2, s63771, sense, 5"-CCAGAACCCAACUCAAUUAtt-3', antisense, 5"-UAAUUGAGUUGGGUUCUGGag-3'.

Co-culture Assay

For the co-culture assays, murine tumor cells and BMSCs were trypsinized, rinsed and re-suspended in 10^5/ml and 10^6/ml density with serum-free DMEM/F12 medium, respectively. For the 2D co-culture assay, 200 tumor cells with or without 5000 BMSCs were seeded into each well of 96-well plate and cultured in serum-free DMEM/F12 medium. For the non-contact co-culture assay, 2000 tumor cells in 1ml medium were seeded in the lower wells of 24-well plate and then incubate for 30 minutes to allow the attachment of cells to the plates. Then, 3E4 BMSCs in 200μl medium were seeded in the upper Transwell Inserts (3.0μm pore size, Greiner Bio-One, Cat# 662630). 0.5X B27 (Thermo Fisher Scientific, Cat# 17504044) was added to sustain the survival of BMSCs in serum free condition. For the 3D co-culture assay, 2E4 tumor cells with or without 2E4 BMSCs were seeded in each well of 24-well low-attachment plate

Downloaded from http://aacrjournals.org/cancerdiscovery/article-pdf/doi/10.1158/2159-8290.CD-22-0220/3217471/cd-22-0220.pdf by Washington University St Louis user on 10 November 2022

(Corning, Cat# 3473) with 1ml serum-free DMEM/F12 medium. The medium was changed every three days. For 2D and non-contact co-culture assays, the cell growth was monitored by Incucyte and quantified the total tumor cell area on day 5 for each well. For the 3D co-culture assay, the fluorescent images of sphere formed in each well were acquired by an Echo Revolve epi-fluorescent microscope (Figure 5B&6E) or Incucyte (others) and the size of sphere was determined by measuring the GFP^+ area by ImageJ. The spheres from same experimental groups were then pooled, and transferred to a 1.5ml Eppendorf tube. After 5-minute centrifugation at 500g, the cell pallets were fixed in 4% PFA for 2 hours and then sent to the pathological core for paraffin embedding and sectioning.

Co-migration Assay

For the co-migration assay, the FluoroBlok inserts with 8 μm pore size (Corning, Cat# 351152) were used. Basically, 1E4 tumor cells with or without 1E4 BMSCs were seeded in the top chambers. 0.6 ml of serum-free DMEM/F12 medium was added in the bottom chambers. Then the migration of tumor cells and BMSCs was monitored by Incucyte. The colored membranes blocked the light transmission, therefore the cells stay in the top chambers were invisible. Once the fluorescently labelled cells migrated through and present under the membrane, cells can be detected.

Bioinformatic Analyses of Human Metastases

GSE14020 (breast), GSE77930 (prostate), GSE101607 (Mixed), and GSE143791 (prostate) were downloaded from the Gene Expression Omnibus database (https://www.ncbi.nlm.nih.gov/geo/). GSE143791 is a single cell RNA-seq dataset. Gene counts were read into the R Statistical Program. Genes with a count number > 1 in a cell were considered expressed by the cells. Co-expression between two genes were evaluated by Fishers' exact tests. The p values of the tests were jointly determined by numbers of cells expressing either genes or number of cells expressing both genes. Therefore, we used the reciprocal of log-transformed p values as an abundance index of cells with multiple properties in Figure 7C&D. Specifically, such index was used for cells expressing both NG2 and pericyte markers (perivascular NG2+ cells) and for cells expressing both CDH2 and osteoblast differentiation signature. When multiple genes were examined against a single gene, the median index of the multiple genes was used. Other datasets are microarray and RNA-seq datasets. Normalized data were read in the R Statistical Program. For individual genes, we used log2-transformed values. For gene signatures, we used single sample Gene Set Enrichment Assay (ssGSEA) implemented by the "gsva" package (62). The signatures used in the analyses were

Downloaded from http://aacrjournals.org/cancerdiscovery/article-pdf/doi/10.1158/2159-8290.CD-22-0220/3217471/cd-22-0220.pdf by Washington University St Louis user on 10 November 2022

specified below. All figures were generated by the "ggplot2" package. Osteoblast differentiation signature, https://www.gsea-msigdb.org/gsea/msigdb/cards/REACTOME_RUNX2_REGULATES_OSTEOBLAST_DIFFERENTIATION.html; Prostate cancer proliferation signature, Cuzick et al. Lancet Oncol (2011) 12(3)245-255 (47); Embryonic stem cell signature expressed in aggressive tumors, https://www.gsea-msigdb.org/gsea/msigdb/cards/BENPORATH_ES_1.html; Estrogen response signature (early), https://www.gsea-msigdb.org/gsea/msigdb/cards/HALLMARK_ESTROGEN_RESPONSE_EARLY.html; Estrogen response signature (late), https://www.gsea-msigdb.org/gsea/msigdb/cards/HALLMARK_ESTROGEN_RESPONSE_LATE.html.

Quantification and Statistical Analysis

If not specified otherwise, all the quantitative data were generated and analyzed by GraphPad Prism 9. Number of animals or independent replicates are denoted in the figure panels or legends. In most *in vivo* experiments, the investigators were blind to the genotype or allocation of subjects until the assessment of outcomes. All the *in vitro* experiments were repeated three times or involved three or more biological replicates. No repeated measurement on the same sample was applied in this study. Preliminary experiments with a small group size were performed to determine the group sizes on each *in vivo* experiment. The final results were pooled from multiple batches of *in vivo* experiments including the preliminary experiments. No animal reached the experimental endpoint were excluded from the final analysis. The statistical methods were noted in the figure legends and two-sided tests were used. Basically, normally distributed data were analyzed with parametric statistics while nonparametric statistics were used for the comparison of metastatic burden, such as bioluminescent intensities and derived data. For comparison of two normally distributed samples, an F-test was performed to assess the variance of two samples. If F-test was rejected, Welch's correction was applied to the Student t-test. P values less than 0.05 were considered as statistically significant.

Data Availability

All the datasets for bioinformatics analysis were downloaded from public database, and the accession numbers are provided in the corresponding figure panels. Numeric values of all figures are provided in Supplementary Raw Data. Other raw data and code are available upon request from the corresponding author.

Downloaded from http://aacrjournals.org/cancerdiscovery/article-pdf/doi/10.1158/2159-8290.CD-22-0220/3217471/cd-22-0220.pdf by Washington University St Louis user on 10 November 2022

ACKNOWLEDGEMENTS

We are grateful to the discussion and suggestions from Zhang Laboratory members. We also thank Dr. Dongsu Park (BCM) and Dr. Yangjin Bae (BCM) for providing relevant animal strains. X.H.-F.Z. is supported by US Department of Defense DAMD W81XWH-16-1-0073 (Era of Hope Scholarship), NCI CA183878, NCI CA251950, DAMD W81XWH-20-1-0375, Breast Cancer Research Foundation, and McNair Medical Institute. S.T.W. and J.L. are supported in part by NCI U01CA252553, John S Dunn Research Foundation, and T.T. and W.F. Chao Center for BRAIN. Y.G. received training support from the Translational Breast Cancer Research Training Program (NIH T32 CA203690, PI: Suzanne Fuqua). This project was supported by the RNA In Situ Hybridization Core with funding from the NIH (1S10OD016167), the Cytometry and Cell Sorting Core with funding from the CPRIT Core Facility Support Award (CPRIT-RP180672), the NIH (P30 CA125123, S10 RR024574, S10 OD025251), the Pathology Core of Lester and Sue Smith Breast Center, the Optical Imaging & Vital Microscopy Core and the Integrated Microscopy core at Baylor College of Medicine, and the MDACC Research Histology Core, and Bone Histomorphometry Core Laboratory at MD Anderson Cancer Center. We also acknowledge Dr. Cecilia Ljungberg, Joy Guo, Rena Mao, and Joel M. Sederstrom at Baylor College of Medicine and Leah Guerra at MD Anderson Cancer Center for their expert assistance.

AUTHOR CONTRIBUTIONS

Conceptualization, W.Z., S.T.W., X.H.-F.Z.; Methodology, W.Z., Z.X., X.H., T.H., H.W., S.T.W., X.H.-F.Z.; Investigation, Formal Analysis and Validation, W.Z., Z.X., X.H., T.H., J. Li, Y.S., K.L., Y.G., J.Liu, D.G.E., A.M.M., L.W., L.Y., L.X., Y.W., I.L.B., Y.D., S.A., H.W.; Resources, X.C., Z.G., R.L.S., S.T.W., X.H.-F.Z.; Software, Data Curation and Visualization, W.Z., T.H., Y.S., X.H.-F.Z.; Writing – Original Draft, W.Z., X.H.-F.Z.; Writing – Review & Editing, W.Z., X.H.-F.Z.; Supervision, S.T.W., X.H.-F.Z.; Project Administration, W.Z., X.H.-F.Z.; Funding Acquisition, S.T.W., X. H.-F. Z.

Downloaded from http://aacrjournals.org/cancerdiscovery/article-pdf/doi/10.1158/2159-8290.CD-22-0220/3217471/cd-22-0220.pdf by Washington University St Louis user on 10 November 2022

REFERENCE

1. Satcher RL, Zhang XHF. Evolving cancer–niche interactions and therapeutic targets during bone metastasis. Nat Rev Cancer [Internet]. 2022 [cited 2021 Dec 27];22:85–101. Available from: https://doi.org/10.1038/

2. Esposito M, Guise T, Kang Y. The biology of bone metastasis. Cold Spring Harb Perspect Med [Internet]. Cold Spring Harbor Laboratory Press; 2018 [cited 2018 Nov 13];8:a031252. Available from: http://perspectivesinmedicine.cshlp.org/

3. Guise TA, Mohammad KS, Clines G, Stebbins EG, Wong DH, Higgins LS, et al. Basic mechanisms responsible for osteolytic and osteoblastic bone metastases. Clin Cancer Res. 2006;12:6213s-6216s.

4. Weilbaecher KN, Guise TA, McCauley LK. Cancer to bone: A fatal attraction. Nat Rev Cancer [Internet]. 2011/05/20. Nature Publishing Group; 2011 [cited 2018 Oct 29];11:411–25. Available from: http://hematology.im.wustl.edu/faculty/weilbaecher/weilbaecherBio.html

5. Zhang W, Bado IL, Hu J, Wan Y-W, Wu L, Wang H, et al. The bone microenvironment invigorates metastatic seeds for further dissemination. Cell [Internet]. Cell Press; 2021 [cited 2021 Apr 19];184:2471-2486.e20. Available from: https://linkinghub.elsevier.com/retrieve/pii/S0092867421002968

6. Guise TA, Yin JJ, Taylor SD, Kumagai Y, Dallas M, Boyce BF, et al. Evidence for a causal role of parathyroid hormone-related protein in the pathogenesis of human breast cancer-mediated osteolysis. J Clin Invest. American Society for Clinical Investigation; 1996;98:1544–9.

7. Kang Y, Siegel PM, Shu W, Drobnjak M, Kakonen SM, Cordón-Cardo C, et al. A multigenic program mediating breast cancer metastasis to bone. Cancer Cell [Internet]. 2003/07/05. Elsevier; 2003 [cited 2018 Oct 29];3:537–49. Available from: http://linkinghub.elsevier.com/retrieve/pii/S1535610803001326

8. Yin JJ, Selander K, Chirgwin JM, Dallas M, Grubbs BG, Wieser R, et al. TGF-beta signaling blockade inhibits PTHrP secretion by breast cancer cells and bone metastases development. J Clin Invest [Internet]. American Society for Clinical Investigation; 1999 [cited 2018 Nov 13];103:197–206. Available from: http://www.ncbi.nlm.nih.gov/pubmed/9916131

Downloaded from http://aacrjournals.org/cancerdiscovery/article-pdf/doi/10.1158/2159-8290.CD-22-0220/3217471/cd-22-0220.pdf by Washington University St Louis user on 10 November 2022

9. Guise TA. Breast cancer bone metastases: It's all about the neighborhood. Cell. 2013;154:957–8.

10. Esposito M, Mondal N, Greco TM, Wei Y, Spadazzi C, Lin SC, et al. Bone vascular niche E-selectin induces mesenchymal–epithelial transition and Wnt activation in cancer cells to promote bone metastasis. Nat Cell Biol [Internet]. Nature Publishing Group; 2019 [cited 2019 Apr 15];21:627–39. Available from: http://www.nature.com/articles/s41556-019-0309-2

11. Wang H, Tian L, Liu J, Goldstein A, Bado I, Zhang W, et al. The Osteogenic Niche Is a Calcium Reservoir of Bone Micrometastases and Confers Unexpected Therapeutic Vulnerability. Cancer Cell [Internet]. Elsevier; 2018 [cited 2018 Nov 12];34:823-839.e7. Available from: https://linkinghub.elsevier.com/retrieve/pii/S1535610818304689

12. Wang H, Yu C, Gao X, Welte T, Muscarella AM, Tian L, et al. The Osteogenic Niche Promotes Early-Stage Bone Colonization of Disseminated Breast Cancer Cells. Cancer Cell [Internet]. Elsevier Inc.; 2015;27:193–210. Available from: http://dx.doi.org/10.1016/j.ccell.2014.11.017

13. Ghajar CM, Peinado H, Mori H, Matei IR, Evason KJ, Brazier H, et al. The perivascular niche regulates breast tumour dormancy. Nat Cell Biol [Internet]. Nature Publishing Group; 2013;15:807–17. Available from: http://dx.doi.org/10.1038/ncb2767

14. Price TT, Burness ML, Sivan A, Warner MJ, Cheng R, Lee CH, et al. Dormant breast cancer micrometastases reside in specific bone marrow niches that regulate their transit to and from bone. Sci Transl Med [Internet]. American Association for the Advancement of Science; 2016 [cited 2018 Oct 22];8:1–12. Available from: https://pubmed.ncbi.nlm.nih.gov/27225183/

15. Bado IL, Zhang W, Hu J, Xu Z, Wang H, Sarkar P, et al. The bone microenvironment increases phenotypic plasticity of ER+ breast cancer cells. Dev Cell [Internet]. Elsevier; 2021 [cited 2021 Apr 19];56:1100-1117.e9. Available from: https://linkinghub.elsevier.com/retrieve/pii/S1534580721002057

16. Clarke B. Normal Bone Anatomy and Physiology. Clin J Am Soc Nephrol [Internet]. American Society of Nephrology; 2008 [cited 2022 Jan 5];3:S131–9. Available from: https://cjasn.asnjournals.org/content/3/Supplement_3/S131

17. Siddiqui JA, Partridge NC. Physiological bone remodeling: Systemic regulation and

Downloaded from http://aacrjournals.org/cancerdiscovery/article-pdf/doi/10.1158/2159-8290.CD-22-0220/3217471/cd-22-0220.pdf by Washington University St Louis user on 10 November 2022

growth factor involvement. Physiology [Internet]. American Physiological Society; 2016 [cited 2022 Jan 5];31:233–45. Available from: https://journals.physiology.org/doi/abs/10.1152/physiol.00061.2014

18. Crane JL, Cao X. Bone marrow mesenchymal stem cells and TGF-β signaling in bone remodeling. J Clin Invest [Internet]. American Society for Clinical Investigation; 2014 [cited 2019 Aug 2];124:466–72. Available from: https://www.jci.org/articles/view/70050

19. Peng Y, Wu S, Li Y, Crane JL. Type H blood vessels in bone modeling and remodeling. Theranostics [Internet]. Ivyspring International Publisher; 2020 [cited 2022 Jan 5];10:426. Available from: /pmc/articles/PMC6929606/

20. Da L, Meirelles S, Caplan AI, Nardi NB. In Search of the In Vivo Identity of Mesenchymal Stem Cells. Stem Cells [Internet]. John Wiley & Sons, Ltd; 2008 [cited 2022 Jan 5];26:2287–99. Available from: https://onlinelibrary.wiley.com/doi/full/10.1634/stemcells.2007-1122

21. Kaigler D, Krebsbach PH, Polverini PJ, Mooney DJ. Role of vascular endothelial growth factor in bone marrow stromal cell modulation of endothelial cells. Tissue Eng [Internet]. Mary Ann Liebert, Inc. ; 2003 [cited 2022 Aug 4];9:95–103. Available from: https://www.liebertpub.com/doi/10.1089/107632703762687573

22. Bertram JS, Janik P. Establishment of a cloned line of Lewis lung carcinoma cells adapted to cell culture. Cancer Lett. Elsevier; 1980;11:63–73.

23. Müller-Brüsselbach S, Kömhoff M, Rieck M, Meissner W, Kaddatz K, Adamkiewicz J, et al. Deregulation of tumor angiogenesis and blockade of tumor growth in PPARβ-deficient mice. EMBO J [Internet]. John Wiley & Sons, Ltd; 2007 [cited 2022 Jan 7];26:3686–98. Available from: https://onlinelibrary.wiley.com/doi/full/10.1038/sj.emboj.7601803

24. Grzelak CA, Goddard ET, Lederer EE, Rajaram K, Dai J, Shor RE, et al. Elimination of fluorescent protein immunogenicity permits modeling of metastasis in immune-competent settings. Cancer Cell [Internet]. 2022 [cited 2021 Dec 6];40:1–2. Available from: https://linkinghub.elsevier.com/retrieve/pii/S1535610821006048

25. Zhou BO, Yue R, Murphy MM, Peyer JG, Morrison SJ. Leptin-receptor-expressing mesenchymal stromal cells represent the main source of bone formed by adult bone marrow. Cell Stem Cell [Internet]. Elsevier Inc.; 2014;15:154–68. Available from: http://dx.doi.org/10.1016/j.stem.2014.06.008

Downloaded from http://aacrjournals.org/cancerdiscovery/article-pdf/doi/10.1158/2159-8290.CD-22-0220/3217471/cd-22-0220.pdf by Washington University St Louis user on 10 November 2022

26. Li Z, Helms JA. Drill Hole Models to Investigate Bone Repair. Methods Mol Biol [Internet]. Humana, New York, NY; 2021 [cited 2022 Jan 5];2221:193–204. Available from: https://link.springer.com/protocol/10.1007/978-1-0716-0989-7_12

27. Ingle BM, Hay SM, Bottjer HM, Eastell R. Changes in Bone Mass and Bone Turnover Following Distal Forearm Fracture. Osteoporos Int 1999 105 [Internet]. Springer; 1999 [cited 2022 Jan 4];10:399–407. Available from: https://link.springer.com/article/10.1007/s001980050246

28. Krall JA, Reinhardt F, Mercury OA, Pattabiraman DR, Brooks MW, Dougan M, et al. The systemic response to surgery triggers the outgrowth of distant immune-controlled tumors in mouse models of dormancy. Sci Transl Med [Internet]. American Association for the Advancement of Science; 2018 [cited 2022 Jan 5];10. Available from: https://www.science.org/doi/abs/10.1126/scitranslmed.aan3464

29. Sivaraj KK, Adams RH. Blood vessel formation and function in bone. Development. The Company of Biologists; 2016;143:2706–15.

30. Yu C, Wang H, Muscarella A, Goldstein A, Zeng HC, Bae Y, et al. Intra-iliac artery injection for efficient and selective modeling of microscopic bone metastasis. J Vis Exp. 2016;2016:1–7.

31. Pinho S, Lacombe J, Hanoun M, Mizoguchi T, Bruns I, Kunisaki Y, et al. PDGFRα and CD51 mark human Nestin $^{+}$ sphere-forming mesenchymal stem cells capable of hematopoietic progenitor cell expansion. J Exp Med [Internet]. 2013;210:1351–67. Available from: http://www.jem.org/lookup/doi/10.1084/jem.20122252

32. Kunisaki Y, Bruns I, Scheiermann C, Ahmed J, Pinho S, Zhang D, et al. Arteriolar niches maintain haematopoietic stem cell quiescence. Nature [Internet]. Nature Publishing Group; 2013 [cited 2018 Nov 1];502:637–43. Available from: http://www.nature.com/articles/nature12612

33. Park D, Spencer JA, Koh BI, Kobayashi T, Fujisaki J, Clemens TL, et al. Endogenous Bone Marrow MSCs Are Dynamic, Fate-Restricted Participants in Bone Maintenance and Regeneration. Cell Stem Cell [Internet]. Cell Press; 2012 [cited 2019 May 31];10:259–72. Available from: https://www.sciencedirect.com/science/article/pii/S1934590912000616#dfig1

34. Sivaraj KK, Jeong HW, Dharmalingam B, Zeuschner D, Adams S, Potente M, et al.

Downloaded from http://aacrjournals.org/cancerdiscovery/article-pdf/doi/10.1158/2159-8290.CD-22-0220/3217471/cd-22-0220.pdf by Washington University St Louis user on 10 November 2022

Regional specialization and fate specification of bone stromal cells in skeletal development. Cell Rep [Internet]. 2021 [cited 2021 Jul 14];36:109352. Available from: http://www.cell.com/article/S2211124721007282/fulltext

35. Abbuehl JP, Tatarova Z, Held W, Huelsken J. Long-Term Engraftment of Primary Bone Marrow Stromal Cells Repairs Niche Damage and Improves Hematopoietic Stem Cell Transplantation. Cell Stem Cell [Internet]. Cell Press; 2017 [cited 2022 Jun 7];21:241-255.e6. Available from: http://www.cell.com/article/S1934590917302837/fulltext

36. Liu S, Liu D, Chen C, Hamamura K, Moshaverinia A, Yang R, et al. MSC transplantation improves osteopenia via epigenetic regulation of notch signaling in lupus. Cell Metab [Internet]. Cell Press; 2015 [cited 2022 May 28];22:606–18. Available from: http://www.cell.com/article/S155041311500409X/fulltext

37. Chang J, Sonoyama W, Wang Z, Jin Q, Zhang C, Krebsbach PH, et al. Noncanonical Wnt-4 signaling enhances bone regeneration of mesenchymal stem cells in craniofacial defects through activation of p38 MAPK. J Biol Chem [Internet]. American Society for Biochemistry and Molecular Biology Inc.; 2007 [cited 2022 Jun 8];282:30938–48. Available from: http://www.jbc.org/article/S0021925820598712/fulltext

38. König MA, Canepa DD, Cadosch D, Casanova E, Heinzelmann M, Rittirsch D, et al. Direct transplantation of native pericytes from adipose tissue: A new perspective to stimulate healing in critical size bone defects. Cytotherapy [Internet]. 2016 [cited 2022 Jun 22];18:41–52. Available from: http://dx.doi.org/10.1016/j.jcyt.2015.10.002

39. Supakul S, Yao K, Ochi H, Shimada T, Hashimoto K, Sunamura S, et al. Pericytes as a Source of Osteogenic Cells in Bone Fracture Healing. Multidisciplinary Digital Publishing Institute; 2019 [cited 2019 Jul 29];20:1079. Available from: http://www.ncbi.nlm.nih.gov/pubmed/30832329

40. Muscarella AM, Dai W, Mitchell PG, Zhang W, Wang H, Jia L, et al. Unique cellular protrusions mediate breast cancer cell migration by tethering to osteogenic cells. npj Breast Cancer [Internet]. 2020 [cited 2020 Sep 12];6:42. Available from: http://www.nature.com/articles/s41523-020-00183-8

41. Marie PJ. Role of N-cadherin in bone formation. J Cell Physiol [Internet]. John Wiley & Sons, Ltd; 2002 [cited 2022 Mar 7];190:297–305. Available from: https://onlinelibrary.wiley.com/doi/full/10.1002/jcp.10073

Downloaded from http://aacrjournals.org/cancerdiscovery/article-pdf/doi/10.1158/2159-8290.CD-22-0220/3217471/cd-22-0220.pdf by Washington University St Louis user on 10 November 2022

42. Di Benedetto A, Watkins M, Grimston S, Salazar V, Donsante C, Mbalaviele G, et al. N-cadherin and cadherin 11 modulate postnatal bone growth and osteoblast differentiation by distinct mechanisms. J Cell Sci [Internet]. The Company of Biologists; 2010 [cited 2022 Jun 15];123:2640–8. Available from: https://journals.biologists.com/jcs/article/123/15/2640/31142/N-cadherin-and-cadherin-11-modulate-postnatal-bone

43. Zhu M, Lin S, Sun Y, Feng Q, Li G, Bian L. Hydrogels functionalized with N-cadherin mimetic peptide enhance osteogenesis of hMSCs by emulating the osteogenic niche. Biomaterials. Elsevier; 2016;77:44–52.

44. Zhao M, Tao F, Venkatraman A, Li Z, Smith SE, Unruh J, et al. N-Cadherin-Expressing Bone and Marrow Stromal Progenitor Cells Maintain Reserve Hematopoietic Stem Cells. Cell Rep. Cell Press; 2019;26:652-669.e6.

45. Kfoury Y, Baryawno N, Severe N, Mei S, Gustafsson K, Hirz T, et al. Human prostate cancer bone metastases have an actionable immunosuppressive microenvironment. Cancer Cell [Internet]. Elsevier Inc.; 2021 [cited 2021 Oct 19];39:1464-1478.e8. Available from: https://doi.org/10.1016/j.ccell.2021.09.005

46. Yamazaki T, Mukouyama YS. Tissue Specific Origin, Development, and Pathological Perspectives of Pericytes. Front Cardiovasc Med. Frontiers Media S.A.; 2018;5:78.

47. Cuzick J, Swanson GP, Fisher G, Brothman AR, Berney DM, Reid JE, et al. Prognostic value of an RNA expression signature derived from cell cycle proliferation genes in patients with prostate cancer: A retrospective study. Lancet Oncol [Internet]. Elsevier; 2011 [cited 2022 Jan 18];12:245–55. Available from: http://www.thelancet.com/article/S1470204510702953/fulltext

48. Subramanian A, Tamayo P, Mootha VK, Mukherjee S, Ebert BL, Gillette MA, et al. Gene set enrichment analysis: A knowledge-based approach for interpreting genome-wide expression profiles. Proc Natl Acad Sci. 2005;102:15545–50.

49. Lin SC, Lee YC, Yu G, Cheng CJ, Zhou X, Chu K, et al. Endothelial-to-Osteoblast Conversion Generates Osteoblastic Metastasis of Prostate Cancer. Dev Cell [Internet]. 2017 [cited 2018 Oct 29];41:467-480.e3. Available from: http://www.ncbi.nlm.nih.gov/pubmed/28586644

50. Méndez-Ferrer S, Scadden DT, Sánchez-Aguilera A. Bone marrow stem cells: current

Downloaded from http://aacrjournals.org/cancerdiscovery/article-pdf/doi/10.1158/2159-8290.CD-22-0220/3217471/cd-22-0220.pdf by Washington University St Louis user on 10 November 2022

and emerging concepts. Ann N Y Acad Sci [Internet]. John Wiley & Sons, Ltd; 2015 [cited 2022 Jan 5];1335:32–44. Available from: https://onlinelibrary.wiley.com/doi/full/10.1111/nyas.12641

51. Zhao M, Li L. Dissecting the bone marrow HSC niches. Cell Res 2016 269 [Internet]. Nature Publishing Group; 2016 [cited 2022 Sep 3];26:975–6. Available from: https://www.nature.com/articles/cr201671

52. Yip RKH, Rimes JS, Capaldo BD, Vaillant F, Mouchemore KA, Pal B, et al. Mammary tumour cells remodel the bone marrow vascular microenvironment to support metastasis. Nat Commun [Internet]. 2021;12:6920. Available from: https://www.nature.com/articles/s41467-021-26556-6

53. Nobre AR, Risson E, Singh DK, Di Martino JS, Cheung JF, Wang J, et al. Bone marrow NG2+/Nestin+ mesenchymal stem cells drive DTC dormancy via TGF-β2. Nat Cancer 2021 23 [Internet]. Nature Publishing Group; 2021 [cited 2022 Jan 5];2:327–39. Available from: https://www.nature.com/articles/s43018-021-00179-8

54. Obi N, Werner S, Thelen F, Becher H, Pantel K. Metastatic Breast Cancer Recurrence after Bone Fractures. Cancers 2022, Vol 14, Page 601 [Internet]. Multidisciplinary Digital Publishing Institute; 2022 [cited 2022 Feb 19];14:601. Available from: https://www.mdpi.com/2072-6694/14/3/601/htm

55. Pfammatter C, Lindenmüller IH, Lugli A, Filippi A, Kühl S. Metastases and primary tumors around dental implants: A literature review and case report of peri-implant pulmonary metastasis. [Internet]. Quintessence Int. 2012 [cited 2022 Jun 1]. page 563–70. Available from: http://www.ncbi.nlm.nih.gov/pubmed/22670251

56. Dib LL, Soares AL, Sandoval RL, Nannmark U. Breast metastasis around dental implants: A case report. Clin Implant Dent Relat Res. Blackwell Publishing Ltd; 2007;9:112–5.

57. Orhan K, Bayndr H, Aksoy S, Seker BK, Berberoğlu A, Ozan O. Numb chin syndrome as a manifestation of possible breast cancer metastasis around dental implants. J Craniofac Surg [Internet]. 2011 [cited 2022 Jun 1];22:942–5. Available from: https://journals.lww.com/jcraniofacialsurgery/Fulltext/2011/05000/Numb_Chin_Syndrome_as_a_Manifestation_of_Possible.40.aspx

58. Favia G, Tempesta A, Limongelli L, Crincoli V, Piattelli A, Maiorano E. Metastatic Breast Cancer in Medication-Related Osteonecrosis Around Mandibular Implants. Am J Case

Downloaded from http://aacrjournals.org/cancerdiscovery/article-pdf/doi/10.1158/2159-8290.CD-22-0220/3217471/cd-22-0220.pdf by Washington University St Louis user on 10 November 2022

Rep. International Scientific Information, Inc.; 2015;16:621–6.

59. Kim IS, Gao Y, Welte T, Wang H, Liu J, Janghorban M, et al. Immuno-subtyping of breast cancer reveals distinct myeloid cell profiles and immunotherapy resistance mechanisms. Nat Cell Biol [Internet]. 2019 [cited 2021 Dec 20];21:1113–26. Available from: https://doi.org/10.1038/s41556-019-0373-7

60. Stirling DR, Swain-Bowden MJ, Lucas AM, Carpenter AE, Cimini BA, Goodman A. CellProfiler 4: improvements in speed, utility and usability. BMC Bioinformatics [Internet]. BioMed Central Ltd; 2021 [cited 2022 Jun 22];22:1–11. Available from: https://bmcbioinformatics.biomedcentral.com/articles/10.1186/s12859-021-04344-9

61. Zhu H, Guo ZK, Jiang XX, Li H, Wang XY, Yao HY, et al. A protocol for isolation and culture of mesenchymal stem cells from mouse compact bone. Nat Protoc [Internet]. Nature Publishing Group; 2010 [cited 2019 Sep 27];5:550–60. Available from: http://dx.doi.org/10.1038/nprot.2009.238

62. Hänzelmann S, Castelo R, Guinney J. GSVA: Gene set variation analysis for microarray and RNA-Seq data. BMC Bioinformatics. 2013;14:7.

Downloaded from http://aacrjournals.org/cancerdiscovery/article-pdf/doi/10.1158/2159-8290.CD-22-0220/3217471/cd-22-0220.pdf by Washington University St Louis user on 10 November 2022

FIGURE LEGENDS

Figure 1. Pathological fractures promote metastatic growth in bone

(A) Schematic diagram of introducing pathological bone fractures in spontaneous metastasis model of LLC1 cells

(B) - (C) Representative *ex vivo* BLI images of right hindlimb bones (**B**) and quantified BLI intensity on both wounded right and unaffected left hindlimb bones (**C**). Red arrows indicate the wounded sites. Sham group, n =16 mice; drill group, n=20 mice; bend group, n=14 mice. 2 and 3 left hindlimb bones were mistakenly not examined in sham and drill group, respectively. Grey dots indicate the samples with BLI intensity below the detection threshold.

(D) Spatial quantification of transformed BLI signals along the right femurs of animals with bone fracture or sham surgeries. The dotted lines indicates the range of standard errors.

(E) - (**F**) Representative immunofluorescent images (**E**) and quantification (**F**) of proliferative tumor cells in drilled and unaffected areas of femurs (n=3 mice). Grey area indicates bone matrix around the drilling site, as determined by the presence of scattered Hoechst+/Ki67-/Endomucin-/GFP- osteocytes. Bone marrow space within 100μm of new bone matrix was considered as fracture areas. Scale bar, 20 μm.

(G) Quantified number of tumor cells at the wounded bone area by flow cytometry analysis.

(H) Percentage of major immune cell populations in femur areas with fracture or sham surgery.

(I) Percentage of osteogenic lineages in $CD45^{-}TER119^{-}CD31^{-}$ stromal cells from the wounded areas of femur bones received sham or fracture surgery, as determined by flow cytometry. Sham group, n =7; drill group, n=8; bend group, n=7 mice.

Data are represented as geometric mean ± geometric SD in **C**; mean ± SEM in **D, F-I**. *P* values were assessed by uncorrected Dunn's test following Kruskal-Wallis test in **C** and **G**; Mann-Whitney test in **D**; Paired Student t test in **F**; Fisher's LSD test following ordinary One-way ANOVA test in **H** and **I**. See also Figure S1.

Downloaded from http://aacrjournals.org/cancerdiscovery/article-pdf/doi/10.1158/2159-8290.CD-22-0220/3217471/cd-22-0220.pdf by Washington University St Louis user on 10 November 2022

Figure 2. NG2$^+$ lineage is required for the initiation of metastatic growth in bones under pathological fracture and homeostatic situation

(A) Schematic diagram and normalized growth curves of intraosseous implantation of tumor cells in either control or lineage depleted mice. 20E4 LLC1 fLuc-EGFP cells were directly injected into femur bones of either WT or Cre expressing mice through intraosseous injection. Each dotted curve represents an individual animal while the highlighted curve shows the mean growth for each group.

(B) Schematic diagram and representative BLI images of spontaneous metastasis in the wounded bones. 20E4 LLC1 fLuc-EGFP cells were implanted subcutaneously to form primary tumors. 18 days later, the primary tumors were surgically removed and bone fracture was introduced on the central shaft of right femur via drilling surgery. Red arrows indicate the wounded sites. n=24 animals for both groups.

(C) Spatial distribution of BLI signals along the wounded femurs of WT and NG2-Cre depleted mice.

(D) Ratio of metastatic involvement on whole right hindlimbs (light red) or around the wounded sites (dark red) in WT and NG2-Cre depleted mice.

(E) Schematic diagram and representative *ex vivo* BLI images of spontaneous metastasis to the right hindlimb bones. WT group, n=21; NG2 depleted group, n=25 mice.

(F) - (G) Quantified total *ex vivo* BLI intensities (**F**) and ratio (**G**) in both right and left hindlimb bones of NG2-Cre depleted and control mice. Grey dots indicate samples without detectable metastasis.

(H) Quantified *ex vivo* BLI intensities of lungs from NG2 lineage depleted and control mice.

(I) Schematic diagram and normalized growth curves of tumor cells in right hindlimbs after intra-iliac artery injection. 5E4 LLC1 fLuc-EGFP cells were directly delivered to the mouse hindlimb bones via intra-iliac artery injection. Dot line box shows the normalized BLI intensities at day 4. Each dotted curve represents an individual animal while the highlighted curve shows the mean growth for each group.

(J) Schematic diagram and normalized bone metastasis growth in NG2 lineage pre-depleted and control mice. NG2+ cells were depleted by diphtheria toxin treatment 10 days before the intra-iliac artery injection of 5E4 LLC1 fLuc-EGFP cells. Each dotted curve represents an individual animal while the highlighted curve shows the mean growth for each group.

Downloaded from http://aacrjournals.org/cancerdiscovery/article-pdf/doi/10.1158/2159-8290.CD-22-0220/3217471/cd-22-0220.pdf by Washington University St Louis user on 10 November 2022

Data are represented as mean ± SEM in **A**, **C**, **I**, and **J;** geometric mean ± geometric SD in **F** and **H**. *P* values were assessed by Fisher's LSD test post repeat measure two-way ANOVA test in **A**, **I** and **J;** by Mann-Whitney test in **C, F** and **H**; by Fisher's exact test in **D;** by Chi-square test in **G**. See also Figure S2.

Downloaded from http://aacrjournals.org/cancerdiscovery/article-pdf/doi/10.1158/2159-8290.CD-22-0220/3217471/cd-22-0220.pdf by Washington University St Louis user on 10 November 2022

Figure 3. NG2$^+$ bone marrow stromal cells directly participate in homeostatic and pathological new bone formation

(A) Schematic diagram showing isolation and *in vitro* culture of NG2-tdRED positive and negative bone mesenchymal stem/stromal cells (BMSCs).

(B) Representative images of *in vitro* trio-lineage differentiation assay of NG2-tdRED positive and negative BMSCs. Three NG2-tdRED$^-$ and four NG2-tdRED$^+$ BMSCs from different animals were used as biological replicates. Scale bars, 20 μm.

(C) - (D) Representative immunofluorescent images of trabecular bones (**C**) and quantified ratio of GFP$^+$tdRED$^+$ versus GFP$^+$ area (**D**) in femurs from NG2-CreER$^+$Rosa-tdTomato$^+$OCN-GFP$^+$ mice after different periods of tamoxifen induction. Green, OCN-GFP; Red, NG2-tdRED; Blue, Hoechst 33342. Scale bars, 100 μm. Each data point represents an individual mouse.

(E) - (F) Representative images (**E**) and percentage of osteoid surface with presence of osteoblasts (**F**) in femurs of NG2 lineage depleted and control mice using Goldner's Trichrome staining. Black arrows indicate osteoid surfaces with osteoblasts. WT, n=7; Dep, n=5 mice. Scale bars, 100 μm.

(G) - (H) Representative images (**G**) and percentage of eroding bone surface (**H**) in femurs of NG2 lineage depleted and control mice by TRAP staining. Red arrows indicate eroding bone surface with osteoclasts. WT, n=7; Dep, n=5 mice. Scale bars, 100 μm.

(I) - (J) Representative confocal images (**I**) and quantified rate (**J**) of new bone formation in NG2 lineage depleted and control mice. WT, n=7; Dep, n=6 mice. Scale bars, 20 μm.

(K) Representative immunofluorescent images of femur bones with pathological fractures in NG2-CreER$^+$Rosa-tdTomato$^+$OCN-GFP$^+$ mice. Green, OCN-GFP; Red, NG2-tdRED; Blue, Hoechst 33342; Grey, Endomucin. n=3 bones for each group. Scale bars, 100 μm.

(L) - (M) Representative microCT images (**L**) and quantified bone volume of callus tissues (**M**) in wounded femurs from Figure 2**B**. n=8 animals per group. Scale bars, 200 μm.

Data are represented as mean ± SEM. P values were calculated by one-way ANOVA test followed by LSD test in D; unpaired Student t test in F, H, J and M. See also Figure S3.

Downloaded from http://aacrjournals.org/cancerdiscovery/article-pdf/doi/10.1158/2159-8290.CD-22-0220/3217471/cd-22-0220.pdf by Washington University St Louis user on 10 November 2022

Figure 4. Spatial distribution of early-stage bone metastases

(A) Representative images of unprocessed and cleared hindlimb bones.

(B) Representative maximum intensity projection images of femur bones with spontaneous metastasis (n=5 animals). Green, LLC1 cells; Red, NG2-tdRED^{+} cells; Blue, vessel. Scale bar, 500 μm for the whole view image and 50 μm for the zoom-in images.

(C) Representative standard deviation projection images of femur bones from IIA models (n=3 animals). NG2 reporter mice received intra-iliac artery injection of 5E4 LLC1 cells and the hindlimb bones were collected 4 days later. Green, LLC1 cells; Red, NG2-tdRED cells; Blue, vessel. Scale bar, 100 μm.

(D) Distribution of GFP+ tumor cells and simulated random spots from the closest NG2^{+} cells in early stage of bone colonization (n=3 animals).

(E) Representative immunofluorescent images of bone sections with NG2+ BM cells and tumor cells at the fracture sites. n=3 animals per group. Green, LLC1 cells; Red, NG2-tdRED cells; Blue, vessel. Scale bar, 100 μm.

Data are represented as mean ± SEM. P values were assessed by Student t test in **D**. See also Figure S4.

Downloaded from http://aacrjournals.org/cancerdiscovery/article-pdf/doi/10.1158/2159-8290.CD-22-0220/3217471/cd-22-0220.pdf by Washington University St Louis user on 10 November 2022

Figure 5. Interaction with NG2+ BMSCs promotes tumor cells growth and migration

(A) Representative fluorescent images of tumor spheres formed by 3D co-culture of murine tumor cells and NG2-tdRED^{+} BMSCs. Scale bars, 100 μm.

(B) Bar graphs showing the growth of tumor spheres under monoculture, co-culture with NG2-tdRED^{-} or NG2-tdRED^{+} BMSCs. The GFP^{+} surface area were normalized to the mean value of spheres in co-culture with NG2-tdRED^{-} BMSCs. Each data point represents an independent replicate using BMSCs pooled from different animals.

(C) - (D) Representative confocal images (**C**) of and quantification (**D**) of Ki67^{hi} or Ki67^{low} tumor cells in heterotypic tumor spheres with BMSCs. Images were acquired by tiled scanning of whole section. The percentage of Ki67^{hi} or Ki67^{low} tumor cells on 6 independent batch of co-culture assays was examined. Green, LLC1 cells; Red, NG2-tdRED^{+} BMSCs; Blue, Hoechst; Grey, Ki67. Scale bars, 100 μm.

(E) - (F) Schematic diagram and representative images (**E**) and quantified size (**F**) of LLC1 tumor colonies in 2D co-culture system. Three biological replicates of NG2-tdRED^{-} BMSCs and four biological replicates of NG2-tdRED^{+} and BMSCs were tested. Scale bars, 400 μm.

(G) - (H) Schematic diagram and representative images (**G**) and quantified fold increases (**H**) of LLC1 or EMT6 tumor cells co-migrated with BMSCs in transwell assay. Scale bars, 100 μm. The total number of migrated tumor cells after 9 hours were counted for each well and normalized to mean value of the monoculture group. Each data point represents a biological replicate of BMSCs.

(I) Heat map showing relative changes of tumor sphere size in 3D co-culture assays with BMSCs. BMSCs were pretreated with osteogenic differentiation medium or normal medium for 7 days. GFP+ area was normalized to the mean value of NG2-tdRED^{-} plus normal medium group and then transformed to Z-score. Three biological replicates of BMSCs per group were tested.

Data are represented as mean ± SEM in **D** and **H**. *P* values were assessed by repeat measure One-way ANOVA followed by LSD test in **B**; by unpaired Student t-test in **D** and **H;** by Nested t-test in **F;** by Two-way ANOVA followed by LSD test in **I**. See also Figure S5 and Supplementary Video 1-3.

Downloaded from http://aacrjournals.org/cancerdiscovery/article-pdf/doi/10.1158/2159-8290.CD-22-0220/3217471/cd-22-0220.pdf by Washington University St Louis user on 10 November 2022

Figure 6. N-Cadherin is required for both the pro-metastasis function and osteogenic differentiation of NG2+ BMSCs

(A) - (B) Representative confocal images (**A**) and quantified rate (**B**) of new bone formation in WT (n=6) and NG2-Cre$^{CDH2\ KO/KO}$ (referred as KO, n=9) mice. Scale bars, 20 μm.

(C) - (D) Representative microCT images (**C**) and quantified bone volume (**D**) of callus tissues from KO (n=5) and WT (n=6) femurs.

(E) Tumor sphere growth in 3D co-culture assays with WT (NG2-tdRED^{+} BMSCs in Figure **5**) or N-Cadherin knockout NG2-tdRED^{+} BMSCs. Each data point represent an independent replicate of co-culture assays using different biological replicates of BMSC. #, same as Fig **5B** (NG2-tdRED^{+} BMSCs).

(F) - (G) Representative confocal images (**F**) and percentage (**G**) of Ki67^{+} or Ki67^{-} LLC1 cells in tumor spheres with WT (n=6 sections) or KO (n=6 sections) BMSCs. Each data point represents the quantified value on each independent section of total six batches of co-culture assays. Images were acquired by tiled scanning. Green, LLC1 cells; Red, BMSCs; Blue, DAPI; Grey, Ki67. Scale bars, 100 μm. #, same as Fig **5D** (NG2-tdRED^{+} BMSCs).

(H) - (I) Representative images (**H**) and quantified surface area (**I**) of LLC1 tumor colonies in 2D co-culture with WT or KO BMSCs. 4 biological replicates of WT BMSCs and 3 biological replicates of KO BMSCs were used and each dot represents an individual tumor colony. Scale bars, 400 μm. #, same as Fig **5F** (NG2-tdRED^{+} BMSCs).

(J) - (K) Representative images (**J**) and quantified increase (**K**) of LLC1 tumor cells co-migrated with WT or KO BMSCs after 9 hours. 4 biological replicates of WT BMSCs and 3 biological replicates of KO BMSCs were used. Scale bars, 100 μm. #, same as Fig **5H** (NG2-tdRED^{+} BMSCs).

(L) Tumor sphere growth in 3D co-culture assay with WT or KO BMSCs pretreated with osteogenic differentiation medium for 7 days. 3 biological replicates of BMSCs were used.

(M) Schematic diagram and normalized growth curve of LLC1 tumor cells in NG2-Cre $^{CDH2\ KO/KO}$ and control mice via intra-osseous implantation. WT, n=8 mice; KO, n=7 mice.

(N) Schematic diagram and representative BLI images of spontaneous metastasis in the wounded bones of WT (n=23) and NG2-Cre $^{KO/KO}$ (n=25) mice. Red arrows indicate the wounded sites.

(O) Spatial distribution of BLI signals along the wounded femurs of WT and NG2-Cre $^{KO/KO}$ mice.

Downloaded from http://aacrjournals.org/cancerdiscovery/article-pdf/doi/10.1158/2159-8290.CD-22-0220/3217471/cd-22-0220.pdf by Washington University St Louis user on 10 November 2022

(P) Ratio of metastatic involvement at the hindlimb bones (light red) or at the drill area (dark red) in WT and NG2-Cre $^{KO/KO}$ mice. P value compares the difference of discernible metastasis in the drill site between two groups.

Data are represented as mean ± SEM in **B**, **D**, **G**, **K**, **L**, **M** and **O**. *P* values were assessed by unpaired student t test in **B**, **D**, **G** and **K**; by paired student t test in **E**; by Nested t test in **I**; by LSD test following repeat measure two-way ANOVA in **M**; by LSD test following ordinary two-way ANOVA in **L**; by Mann-Whitney test in **O**; by Fisher's exact test in **P**. See also Figure S6 and Supplementary Video 4.

Downloaded from http://aacrjournals.org/cancerdiscovery/article-pdf/doi/10.1158/2159-8290.CD-22-0220/3217471/cd-22-0220.pdf by Washington University St Louis user on 10 November 2022

Figure 7. Correlative analysis of NG2 (CSPG4) expression in human bone metastases.

(A) Representative confocal images of human bone metastasis samples co-stained with cytokeratin 8/19 (Magenta), NG2 (Red) and N-cadherin (Green). Breast cancer, n=2; Colon cancer, n=1; Prostate cancer, n=2; Lung cancer, n=1. Scale bar, 20μm.

(B) Boxplots show gene expression of NG2 in GSE143791 dataset as reads per million transcripts (RPM). The p value was determined by one-way ANOVA.

(C) A heatmap shows the co-expression of NG2 with indicated genes as evaluated by p values of the Fisher's exact test. A value of 13 (indicated) is corresponding to $p < 0.0005$ or adjusted p value of 0.05 after the Bonferroni correction.

(D) Scatter plots show the correlation between NG2+ perivascular cells and a tumor-specific proliferation index (see Methods). A.U.: arbitrary unit. P values was determined by Spearman correlation analysis.

(E) Scatter plots show the correlation between NG2+ perivascular cells and a CDH2-related osteogenic index (see Methods). A.U.: arbitrary unit. P values was determined by Spearman correlation analysis.

(F) A heatmap shows the expression of indicated individual genes or signatures (sig.). Samples are ordered by CSPG4 expression. **: P = 0.0086 by Spearman correlation analysis.

(G) Boxplots show CSPG4 expression between AR-driven and non-PR-driven tumors. P values were assessed by Mann-Whitney test. See also Figure S7.

Downloaded from http://aacrjournals.org/cancerdiscovery/article-pdf/doi/10.1158/2159-8290.CD-22-0220/3217471/cd-22-0220.pdf by Washington University St Louis user on 10 November 2022

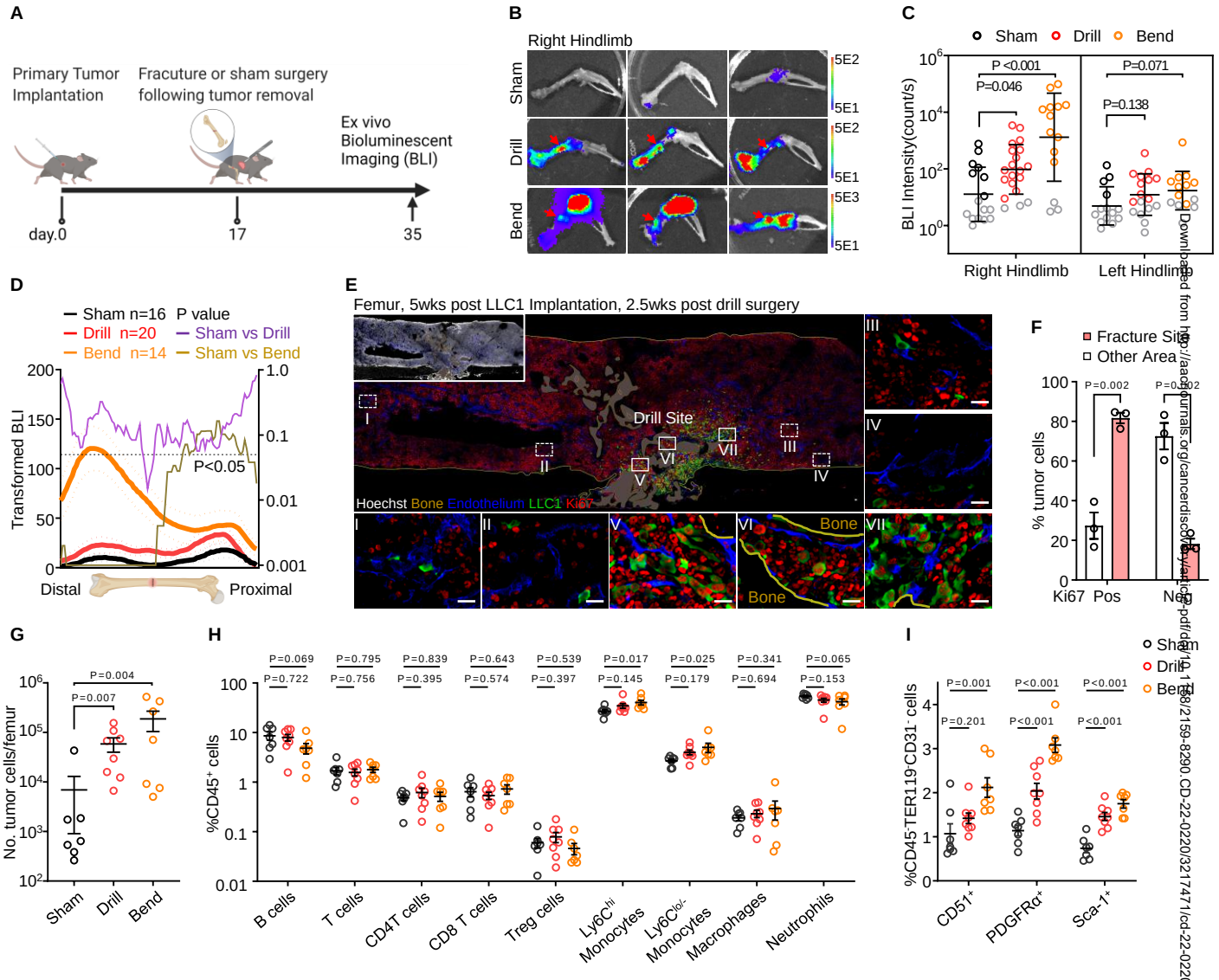

Figure 1. Pathological fractures promote metastatic growth in bone

Downloaded from http://aacrjournals.org/cancerdiscovery/article-pdf/doi/10.1158/2159-8290.CD-22-0220/3217471/cd-22-0220.pdf by Washington University St Louis user on 10 November 2022

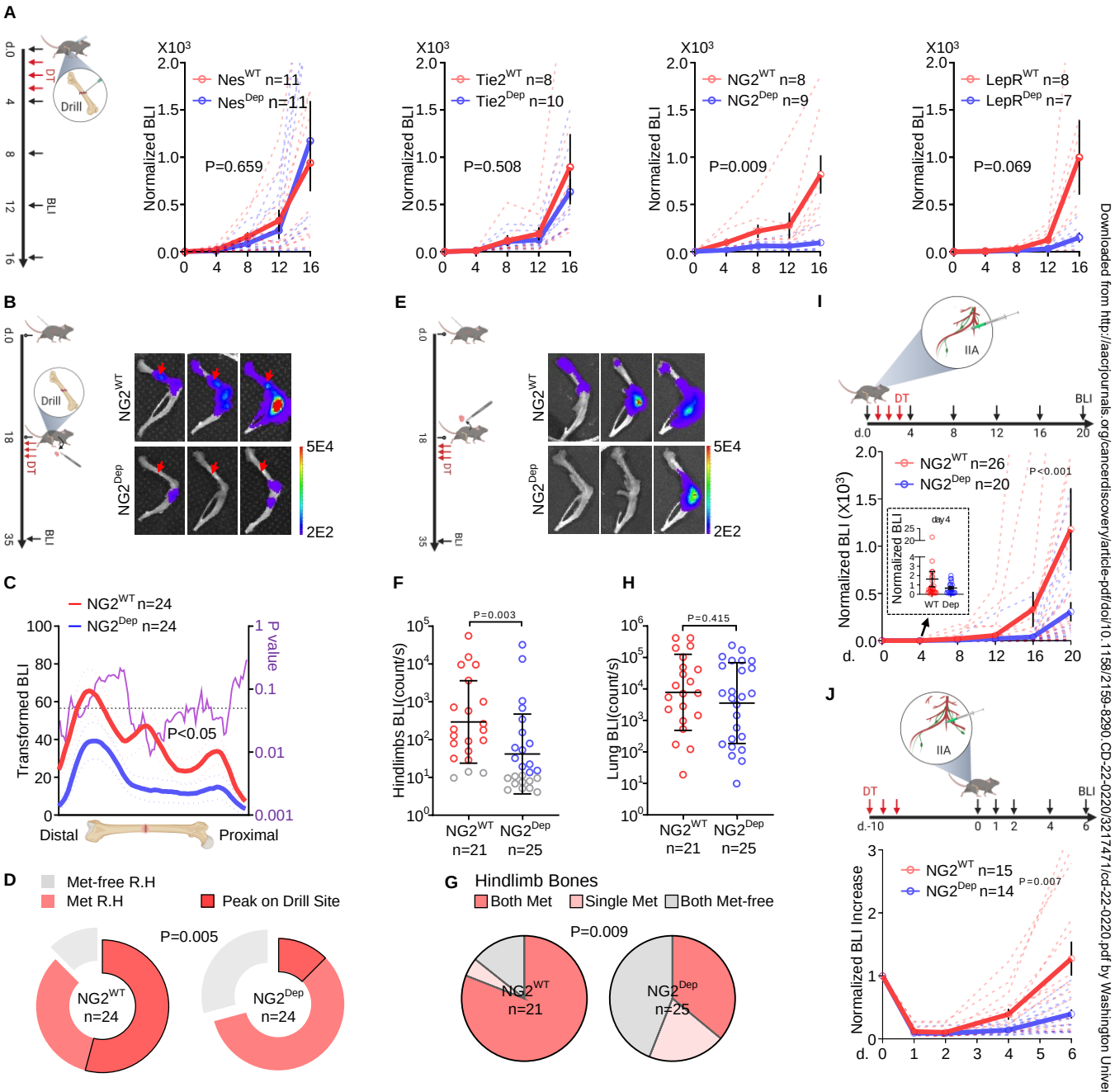

Figure 2. NG2⁺ lineage is required for the initiation of metastatic growth in bones under pathological fracture and homeostatic situation

Downloaded from http://aacrjournals.org/cancerdiscovery/article-pdf/doi/10.1158/2159-8290.CD-22-0220/3217471/cd-22-0220.pdf by Washington University St Louis user on 10 November 2022

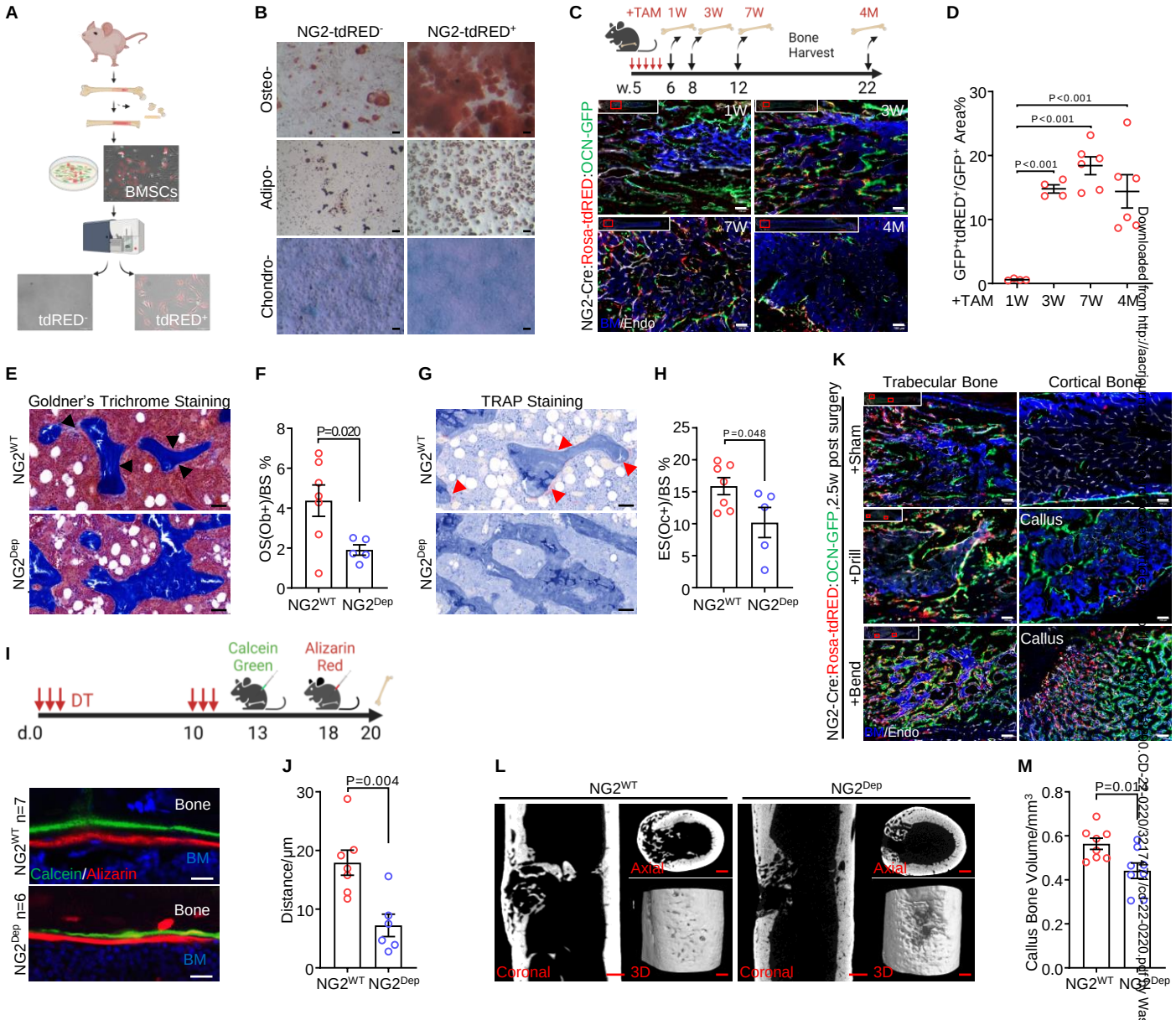

Figure 3. NG2⁺ bone marrow stromal cells directly participate in homeostatic and pathological new bone formation

Downloaded from http://aacrjournals.org/cancerres/article-pdf/doi/10.1158/0008-5472.CD-22-0220/3217477/cd-22-0220.pdf by Washington University St Louis user on 10 November 2022

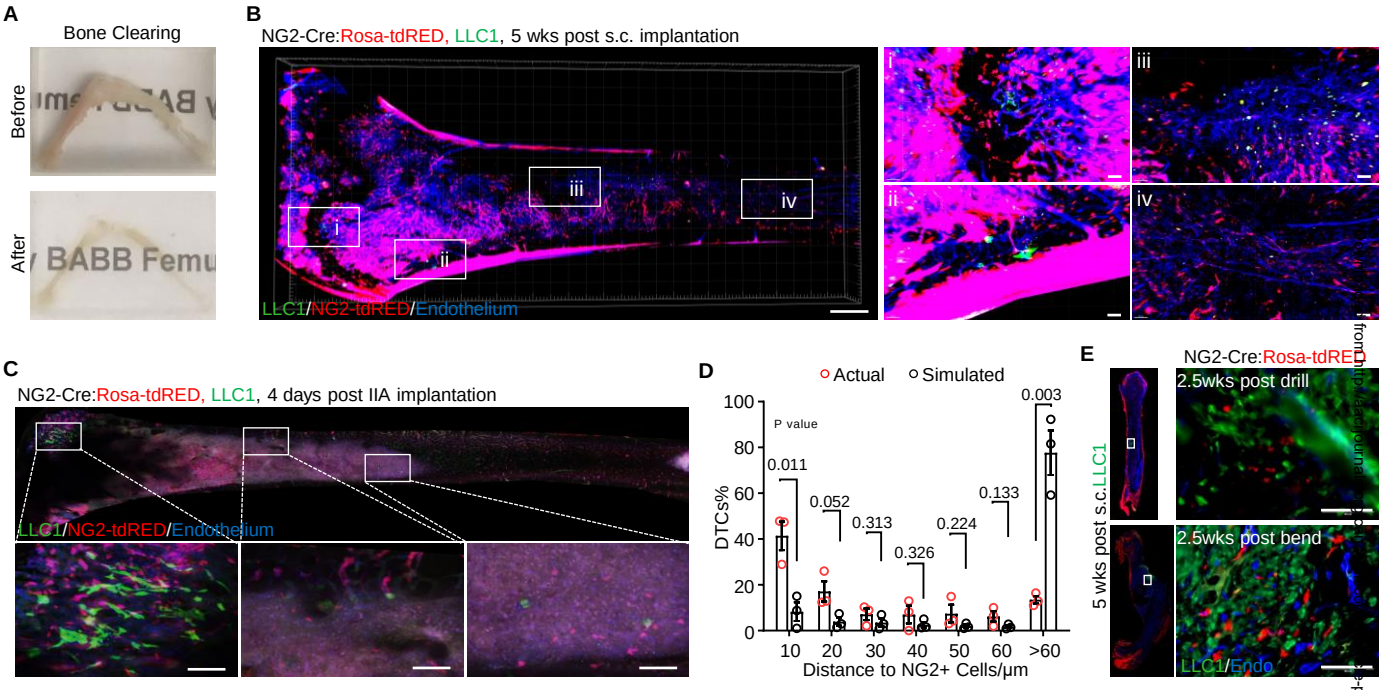

Figure 4. Spatial distribution of early-stage bone metastases

from http://aacrjournals.org/cancerdiscov/article-pdf/doi/10.1158/2159-8290.CD-22-0220/3217471/cd-22-0220.pdf by Washington University St Louis user on 10 November 2022

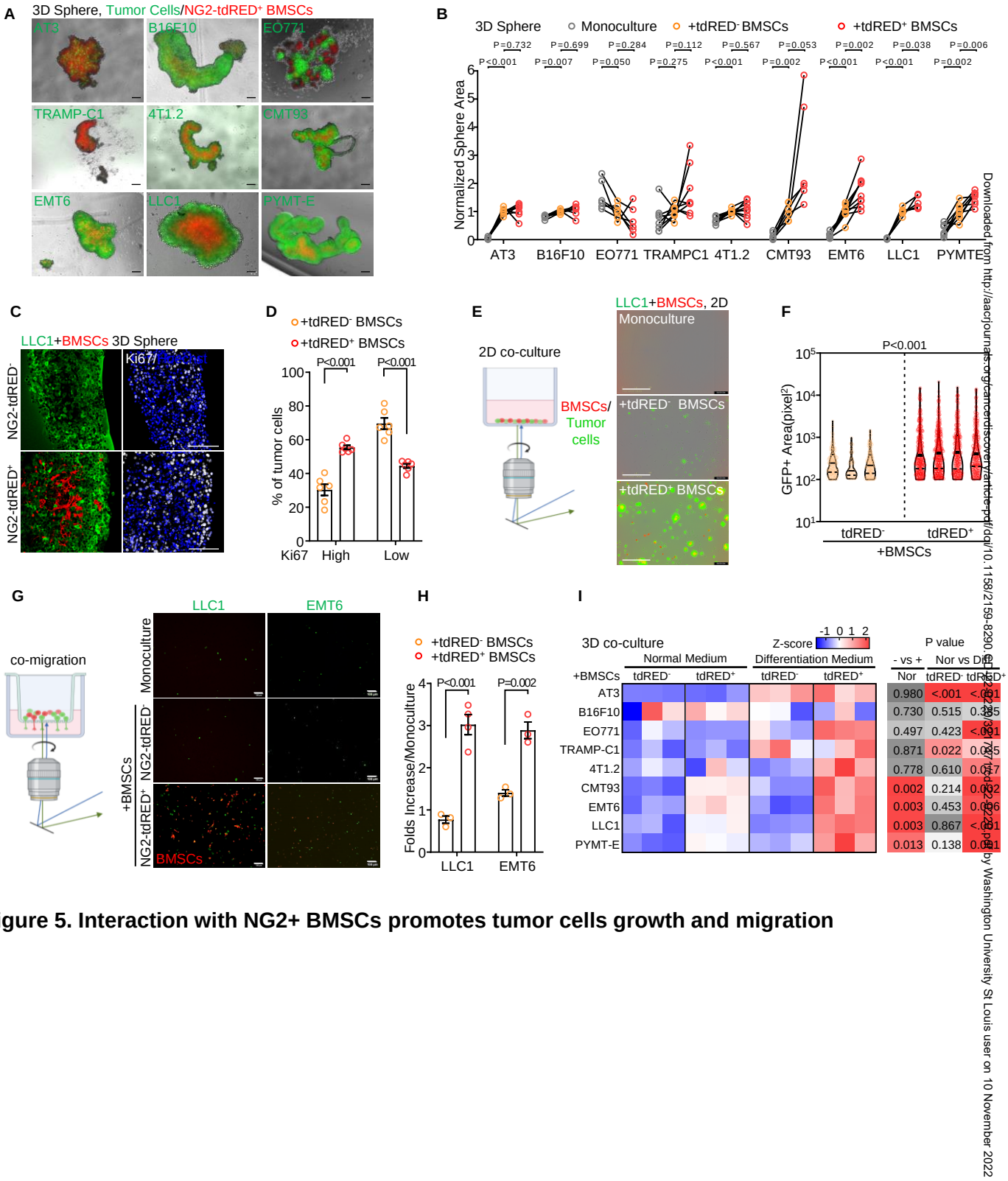

Figure 5. Interaction with NG2+ BMSCs promotes tumor cells growth and migration

Downloaded from http://aacrjournals.org/cancerdiscovery/article-pdf/doi/10.1158/2159-8290.CD-22-0323/3076422/cd-22-0323.pdf by Washington University St Louis user on 10 November 2022

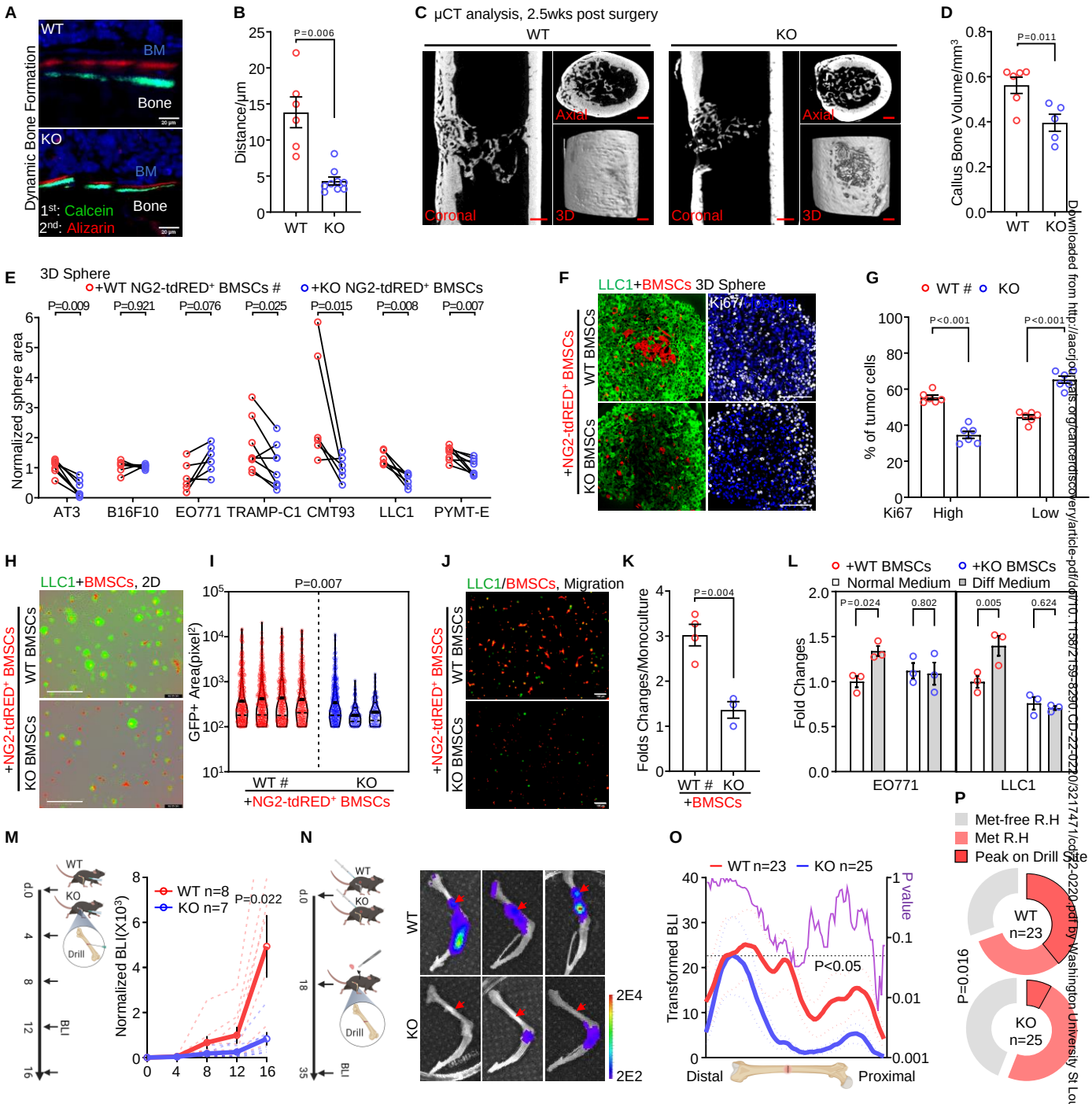

Figure 6. N-Cadherin is required for both the pro-metastasis function and osteogenic differentiation of NG2+ BMSCs

Downloaded from http://aacrjournals.org/cancerdiscovery/article-pdf/doi/10.1158/2159-8290.CD-22-0220/3217471/cd-22-0220.pdf by Washington University St Louis user on 10 November 2022

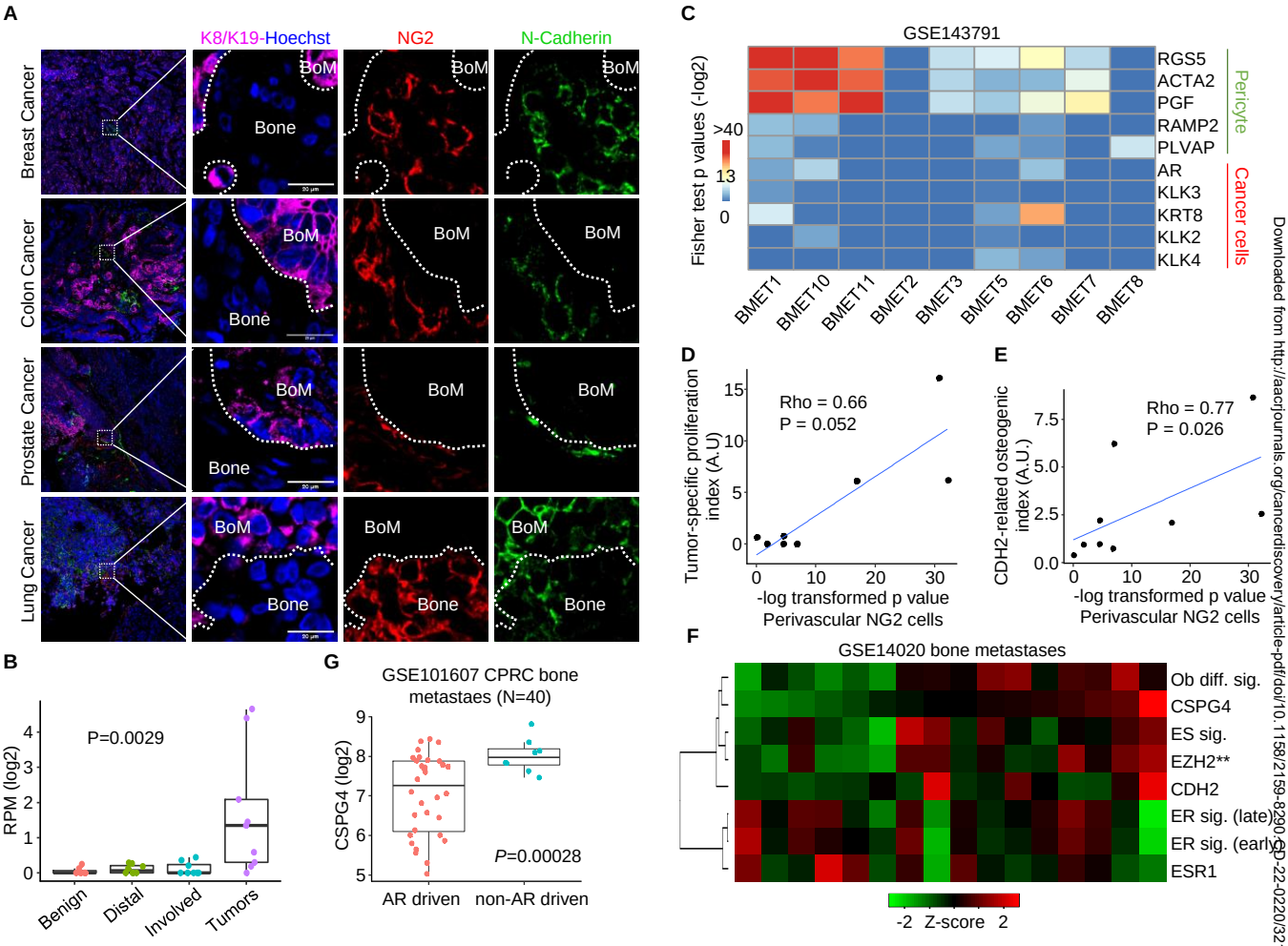

Figure 7. Correlative analysis of NG2 (CSPG4) expression in human bone metastases

Downloaded from http://aacrjournals.org/cancerdiscovery/article-pdf/doi/10.1158/2159-8290.CD-22-0220/3217471/cd-22-0220.pdf by Washington University St Louis user on 10 November 2022